


Multi-omics identify hallmark protein and lipid features of small extracellular vesicles circulating in human plasma

Received: 16 March 2024

Accepted: 26 September 2025

Published online: 28 November 2025

 Check for updates

Alin Rai^{1,2,3}✉, Kevin Huynh^{1,2,3}, Jonathon Cross¹, Qi Hui Poh¹, Haoyun Fang^{1,2}, Bethany Claridge¹, Thy Duong¹, Carla Duarte¹, Jonathan E. Shaw^{1,3,4}, Thomas H. Marwick^{1,2,3}, Peter Meikle^{1,2,3} & David W. Greening^{1,2,3}✉

Extracellular vesicles (EVs) are an essential signalling entity in human plasma implicated in health and disease. Still, their core protein and lipid componentry, which lie at the centre of EV form and function, remain poorly defined. Here we performed high-resolution density gradient fractionation of over 140 human plasma samples to isolate circulating EVs, and systematically constructed their quantitative proteome (4,500 proteins) and lipidome (829 lipids) landscapes using mass spectrometry. We identified a highly conserved panel of 182 proteins (including ADAM10, STEAP23 and STX7) and 52 lipids (including PS, PIPs, Hex2Cer and PAs), providing a deep survey of hallmark molecular features and biological pathways characteristic to circulating EVs. We also mapped the surfaceome diversity, identifying 151 proteins on the EV surface. We further established a set of 42 proteins and 114 lipids features that served as hallmark features of non-EV particles in plasma. We submit ADAM10 and PS(36:1) as conserved EV biological markers that precisely differentiate between EV and non-EV particles. Our findings, which can be explored via an open-source Shiny web tool (evmap.shinyapps.io/evmap/), will serve as a valuable repository to the research community for a clearer understanding of circulating EV biology.

Extracellular vesicles (EVs) are membrane-enclosed nanoscale particles (30–1,000 nm in diameter) released by cells into their extracellular space^{1,2}. By transferring bioactive cargo such as proteins, lipids, nucleic acids and metabolites between cells^{3–6}, EVs execute diverse biological functions in various physiological and pathological processes. EVs are also found ubiquitously in the human circulatory system^{7–15}, with an estimated 50×10^6 particles per millilitre of plasma⁹, and are now recognized as an essential signalling entity in human plasma. While their precise functions in humans remain mostly elusive, circulating EVs have been implicated in essential life processes, including immune

regulation¹⁶, interorgan crosstalk^{17,18}, tissue homeostasis and regeneration¹⁹ and coordinating physiological responses^{20–22}. Dysregulation of their cargo composition is also implicated in various human diseases such as cancer²³, cardiovascular disease²⁴, artery calcification²⁰ and coronavirus disease 2019 pathogenesis²⁵. As minimally invasive liquid biopsies, they have also garnered interest for their potential diagnostic value⁹ and real-time monitoring of therapeutic response^{26,27}.

Despite their wide biological and biomedical implications, the study of circulating EVs remains exceptionally challenging²⁸, with their conserved protein and lipid composition still poorly

¹Baker Heart and Diabetes Institute, Melbourne, Victoria, Australia. ²Baker Department of Cardiometabolic Health, University of Melbourne, Melbourne, Victoria, Australia. ³Baker Department of Cardiovascular Research Translation and Implementation, La Trobe University, Melbourne, Victoria, Australia.

⁴School of Public Health and Preventive Medicine, Monash University, Melbourne, Victoria, Australia. ✉e-mail: alin.rai@baker.edu.au; david.greening@baker.edu.au

characterized—representing an unmet milestone in the field. Given that conserved molecular blueprint epicentres form and function of a biological system—sharing unique proximity to phenotype and pathophysiology²⁹—closing this knowledge gap is critical for advancing our fundamental understanding of circulating EVs and harnessing their clinical potential. Recently, while several seminal studies^{30,31} have begun to define the precise core of EVs using *in vitro* culture systems, making such discoveries for EVs circulating in human plasma remains a formidable challenge. This is mainly due to the presence of large abundance of non-EV components (such as lipoprotein particles, soluble proteins, complement proteins and immunoglobulins) in plasma that outnumber EVs by six to seven orders of magnitude³². Such non-EV particles copurify with EVs, which invariably limits mass spectrometry (MS)-based quantifications primarily to high-abundant plasma proteins or lipoproteins particle-associated lipids, resulting in incomplete and low-coverage data^{14,23,25}. Thus, there is an ongoing international effort within the EV community^{9,11,31,33–35} to develop and refine plasma EV (pEV) isolation methods, with the aim of precisely defining their molecular landscape^{10,12,14,36,37}.

A systematic construction of the conserved protein and lipid componentry of circulating EVs in humans has several implications. It will inform us on fundamental building blocks of circulating EVs, providing high-confidence molecular maps and associated biological pathways such as biogenesis (including membrane curvature, stability and cargo recruitment), release, environmental interactions and uptake mechanisms in humans. Given that existing EV markers obtained from cell culture systems have limited conservation in humans²³—potentially due to unique architecture and context of human tissues^{38,39}—these conserved features will also serve as robust EV markers applicable to human plasma that can be rigorously implemented in large-scale population studies, advance EV purification and characterization techniques, and extend international EV guidelines²⁸ for standardized circulation EV research. In addition, these conserved features will bridge the knowledge gap between humans and cultures/animal models, enhancing knowledge transferability and translatability. Other implications include informing on strategies for engineering and functionalizing EV membranes for improved drug delivery vehicles (for example, extended half-life in circulation), and developing safer EV-based therapies.

In this study, we used high-resolution density gradient separation (DGS) to isolate a major EV subtype, known as small EVs, from human plasma. We verify the enrichment strategy and EV identity using various biochemical and biophysical characterization, ensuring a high degree of separation of EVs and non-EV particles in plasma. We then construct their detailed proteome and lipidome maps, identifying 182 proteins and 52 lipids as core protein and lipid componentry of EVs, which we refer to as EV hallmark features. We also identify 29 proteins and 114

lipids that are defining features of non-EV particles. These markers, in particular ADAM10 and PS(36:1), enable precise differentiation between EV and non-EV particles using machine learning. To enhance data accessibility, we developed an open-source R/Shiny web tool (evmap.shinyapps.io/evmap/).

Results

Isolation of circulating EVs from human plasma

While there is no method that can isolate EVs to absolute purity, high-resolution iodixanol-based DGS^{40–42} remains a powerful strategy for enriching EVs from complex biofluids such as plasma. To this end, we subjected plasma to top-down DGS (Fig. 1a,b), which resolved the majority of signals for abundant plasma components such as albumin, apolipoproteins and argonaut 2 (AGO2, known to associate with non-EV RNA extracellularly⁴³) to DGS fractions 1–5. By contrast, CD63 (tetraspanins that are found in small EVs) resolved in DGS fractions 6–8 (corresponding to flotation buoyancy of -1.09 g ml^{-1} , typical of EVs) (Fig. 1a,b). This level of resolution was not achievable with ultracentrifugation alone (100,000g, referred to as p100K), which co-isolated large amounts of abundant plasma components (Fig. 1c and Supplementary Fig. 1a).

EV particles in DGS 6–8 fractions (pEVs) were morphologically intact, membrane-limited spherical vesicles, consistent with previous reports^{44–47} (Fig. 1d), with a mean diameter of 220.4 nm (Supplementary Fig. 1b). By contrast, the p100K fraction contained abundant proteinaceous material that formed aggregates, whereas DGS 1–3, referred to as pDGS.LD (plasma DGS light-density particles), contained spherical structures lacking an apparent lipid membrane—resembling the size and morphology of lipoprotein particles⁸.

Moreover, nanoparticle tracking analysis (Fig. 1e) revealed that pEVs ranged from 30 to 300 nm in size and displayed a net negative charge (Fig. 1f), consistent with a previous report⁴⁸. Thus, our data show that we can successfully enrich for small EVs from human plasma with minimal contamination from non-EV plasma components. We further demonstrate EV enrichment from multiple plasma samples (Supplementary Fig. 1c,d). From 1 ml of plasma, we obtained $\sim 8.7 \mu\text{g}$ of pEVs (a striking $>24,000$ fold reduction compared with total plasma protein) (Supplementary Fig. 1e), corresponding to $\sim 4.2 \times 10^9$ particles (Supplementary Fig. 1f,g). To assess separation efficiency, we also performed bottom-loaded DGS by carefully loading plasma at the bottom of the gradient before ultracentrifugation (Supplementary Fig. 1h). While EVs were recovered in similar fractions as in the top-loaded approach (cluster of differentiation (CD)63 signal in fraction 6), bottom-loaded DGS resulted in greater cofractionation of non-EV components, including ALB and APOA1, across multiple fractions. This suggests that, compared with top-loaded DGS, bottom-loaded DGS does not achieve the same resolution in plasma samples.

Fig. 1 | Mapping the core proteome of circulating EVs in human plasmas.

a, Workflow for DGS of human plasma (0.5 ml) for EV isolation and characterization. **b**, Western blot analysis of 12 DGS fractions (vol:vol matched) of human plasma with antibodies against indicated proteins. **c**, Western blot analysis of unprocessed plasma, p100K and DGS fractions 6–8 (pooled). **d**, Cryogenic electron microscopic images of p100K, DGS fractions 1–3 and 6–8. Scale bar, 500 nm ($n = 3$, independent plasma samples). **e**, Size distribution (particle diameter (nm)) of plasma DGS fractions 1–3 and 6–8 ($n = 7$, independent plasma samples) based on nanoparticle tracking analysis. Small EVs released by SW620 cells (*in vitro* EVs ($n = 5$, biological replicates)) were also analysed. **f**, The zeta potential of DGS fractions 1–3 and 6–8 at 11 positions throughout the sample cell (top), or stationary layers in the sample cell (bottom) ($n = 8$ for pDGS.LD and $n = 7$ for pEVs, independent samples). The boxplot show the median (centre line), 25th–75th percentiles (box), minima and maxima within $1.5 \times$ interquartile range (whiskers) and outliers beyond. **g**, Proteome landscape construction of pEVs ($n = 38$ independent plasma samples, 5 independent isolation sets; Supplementary Fig. 2) and NonEVs ($n = 42$, independent plasma

samples). **h**, PCA of quantified proteins in pEVs and NonEVs. **i**, Occurrence analysis of proteins in 38 pEV proteomes where category 1 proteins represent ubiquitously quantified proteins. GO pathways enriched (Benjamini–Hochberg-corrected adjusted P value < 0.05) in each category of proteins are indicated. **j**, Scatter plot representing differential abundance ($P < 0.05$) of category 1–3 proteins in pEVs compared with NonEVs. Two-sided t -tests were used to compare protein abundances between pEVs and non-EVs. Proteins with $P < 0.05$ are shown. Multiple-comparison adjustment (Benjamini–Hochberg FDR) was applied, and adjusted values are reported in Supplementary Table 7. **k**, KEGG pathways enriched in pEV or NonEV protein features. Molecular Function GO terms enriched for each protein list were computed using a two-sided hypergeometric test. P values were adjusted for multiple testing with Benjamini–Hochberg (reported as adjusted P values; cut-off 0.05). **l**, Surface-accessible category 1 proteins of pEVs categorized based on their molecular/functional annotation. C/R/T represents clusters of differentiation (CDs), receptors and transporters. The heatmap shows the abundance of the indicated proteins in pEVs ($n = 9$, independent plasma samples) and *in vitro* EVs ($n = 3$, biological replicates).



Constructing the proteome draft of circulating EVs in humans

We next performed MS-based proteomics analysis of pEVs from 38 human plasma samples from multiple sources (Supplementary Fig. 2a). To identify EV-specific proteins, we compared the pEV proteomes with those of pDGS.LD, p100K and unprocessed plasma, collectively termed as NonEVs ($n = 42$) (Fig. 1g, Supplementary Fig. 2b and Supplementary Tables 1–6). Using stringent peptide and protein identification criterion (1% false discovery rate, FDR), we quantified 4,631 proteins in pEVs and 1,678 in NonEVs (Supplementary Fig. 2c and Supplementary Table 6). The size of pEV proteome dataset was comparable to those obtained for in vitro EV proteome data from four different cell lines (4,492 proteins), ensuring sufficient proteome coverage.

The pEV proteome displayed a remarkable dynamic range (Supplementary Fig. 2d), including extensive coverage of low-abundant circulating proteins⁴⁹ (Supplementary Fig. 2e), and was distinct to the NonEV proteome (Fig. 1h and Supplementary Fig. 2f). Moreover, differentially abundant proteins in pEVs were enriched for terms/pathways associated with small EVs (regulation of actin cytoskeleton and endocytosis) (Supplementary Fig. 3a–c and Supplementary Tables 7 and 8) and EV biogenesis proteins^{30,45,47,50,51} (Supplementary Fig. 3d). By contrast, NonEVs contained components related to complement and coagulation pathways, along with abundant plasma proteins⁵² (Supplementary Fig. 3a–d), further supporting our EV enrichment pipeline at omics level. Importantly, although activated platelet EV proteins such as CLEC1B, PF4 and PPBP (which we previously reported⁵³) contribute towards the pEV proteome landscape (Supplementary Fig. 4 and Supplementary Table 9), we observed an abundance of non-platelet EV proteins (Extended Data Fig. 1a–c), suggesting that the pEV proteome represents a diverse cellular source^{15,54,55} (Extended Data Fig. 1d,e and Supplementary Table 10). Indeed, we quantified diverse cell-, tissue- and organ-associated proteins in pEVs^{56,57}, suggesting that our dataset provides a snapshot of the diverse vesicular population in circulation (Extended Data Fig. 2a–d and Supplementary Table 11): many of these cell signatures were also enriched in pEVs versus NonEVs (Extended Data Fig. 2e,f and Supplementary Table 12). Furthermore, our high-resolution MS quantified low-abundant but biologically functional molecules in pEVs, including signal transduction proteins, cytokines and chemokines, kinases⁵⁸, cell-surface receptors, transporters and CD proteins⁵⁹, RNA-binding proteins⁶⁰, and transcription factors⁶¹ (Extended Data Fig. 3a–b, Supplementary Table 11). These include RNA binding proteins such as HNRNPK⁶² and PCBP2⁶³, TFs such as NME2⁶⁴, kinases such as SRC⁶⁵, chemokines such as TGFBI⁶⁶, and receptors such as integrins⁶⁷, previously reported to be functionally active cargo of EVs. These molecules (for example, cytokines) exhibit abundances comparable to canonical CD proteins typical of EVs, strongly supporting their active incorporation (Extended Data Fig. 3c,d).

Defining the core protein features of circulating EVs

Echoing a recent report²³, although several EV proteins (namely 22 core proteins reported in in vitro EVs³⁰ and 94 EV marker proteins

recommended by the minimal information for studies of extracellular vesicles (MISEV) guidelines^{28,36}) were detected in pEVs (Supplementary Fig. 5a and Supplementary Table 6), many were not universally quantified (Supplementary Fig. 5b–d).

Meanwhile, occurrence analysis identified 259 proteins ubiquitously quantified in all 38 pEV samples (termed category 1 proteins; Fig. 1i and Supplementary Table 7); these proteins were enriched for EV-related terms and processes (Extended Data Fig. 4a and Supplementary Table 13) and encompass proteins associated with endosomal trafficking network (Extended Data Fig. 4b) such as flotillins, integrins and CD proteins, whose close interconnectedness is highlighted by their protein–protein interaction network (Extended Data Fig. 4c).

For pEV protein feature selection, we first selected proteins that were 100% conserved in pEV proteomes (that is, present in all 38 proteome datasets, category 1 proteins), which resulted in 259 proteins. Next, of these 259 proteins, we selected proteins with fold change >1.5 and P value <0.0001 in pEV versus NonEVs, resulting in 182 proteins, which we refer to as pEV protein features (Fig. 1j, Extended Data Fig. 5a and Supplementary Table 7; FDR <0.05, as reported in Supplementary Table 20).

For NonEV protein feature selection, we first selected proteins that were 100% conserved in NonEV proteomes (that is, present in all 42 proteome datasets), which resulted in 114 proteins. Next, of these 114 proteins, we selected proteins with fold change <−1.5 and P value <0.0001 in pEV versus NonEVs, resulting in 42 proteins, which we refer to as NonEV protein features (Extended Data Fig. 5b,c and Supplementary Table 7; FDR <0.05, as reported in Supplementary Table 20).

Emphasizing their significance as essential EV components, the pEV protein features were enriched for classical EV pathways (Fig. 1k and Supplementary Table 14). These pEV protein features showed coordinated molecular patterns across functional groups associated with ‘vesicular transport’, ‘actin cytoskeleton regulation’ and ‘membrane-raft assembly’ (see Extended Data Fig. 6a for enrichment-based associations). Upon closer inspection, these correlated molecular patterns were conserved across individual EV proteomes at the cellular level or within specific EV subpopulations (that is, CD9/CD81/CD63-positive EVs) (Extended Data Fig. 6b and Supplementary Table 15). Moreover, these enrichment trends were observed in EVs from primary human fibroblasts (Extended Data Fig. 6c) and were enriched in EVs relative to parental cell proteomes³⁰ (Extended Data Fig. 6d). By contrast, NonEV protein features were enriched for ‘endopeptidase inhibitor activity’, ‘complement and coagulation cascades’ and ‘cholesterol metabolism’ (Fig. 1k and Supplementary Table 14).

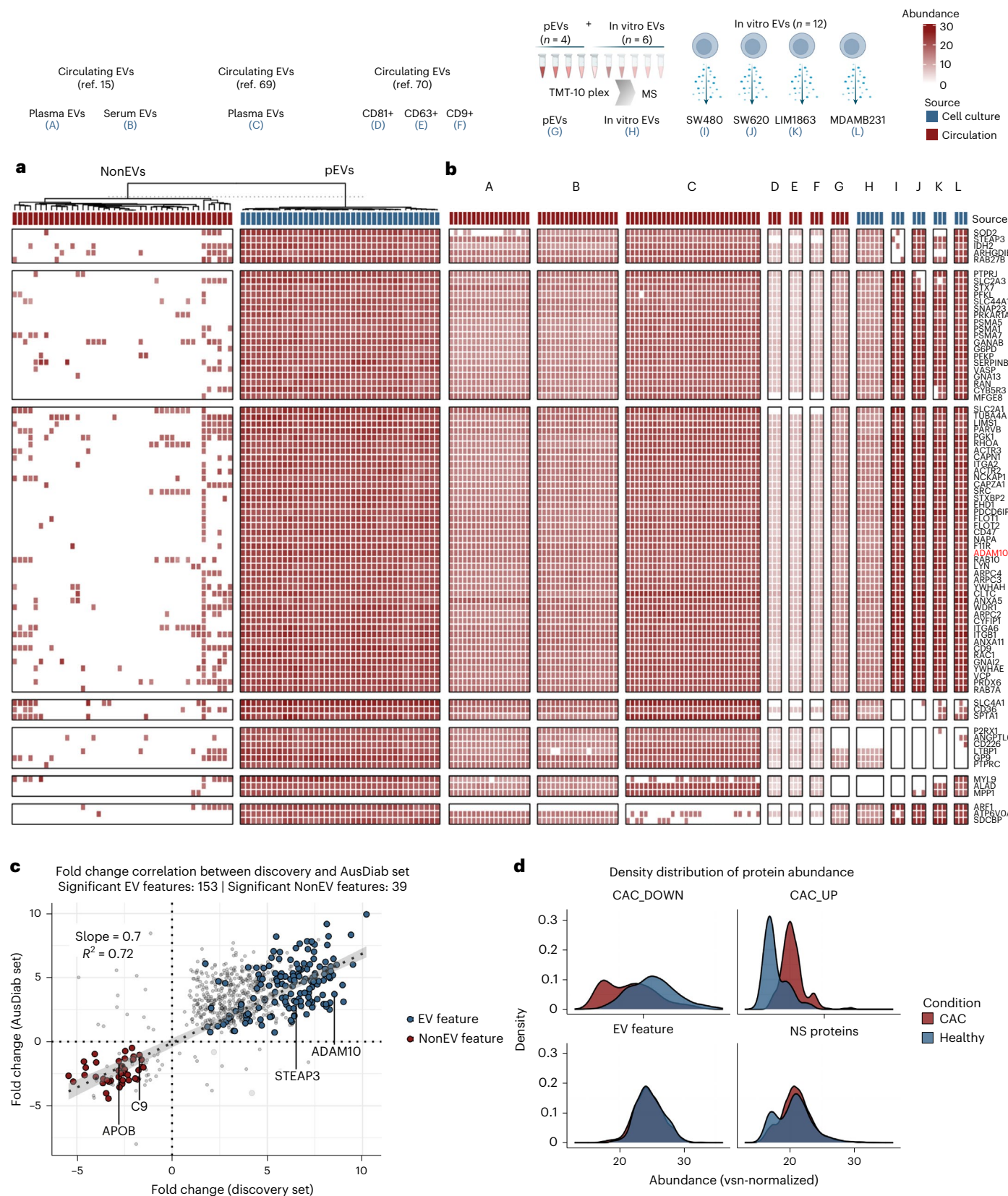
We next investigated whether the pEV protein features also include the EV surfaceome, the essential interactive platform on EV surfaces⁶⁸. To explore this, surface-accessible proteins on pEV were labelled with membrane-impermeant Sulfo-NHS-SS-Biotin, captured with avidin-coated beads and analysed through MS-based proteome profiling ($n = 9$) (Supplementary Fig. 6a and Supplementary Table 16). Our data revealed that 151 pEV protein features were surface-accessible, including CD proteins (CD44 and CD47), integrins (ITGA2, ITGA6 and

Fig. 2 | Conservation of circulating EV protein features. **a**, A heatmap depicting the quantification of EV protein features in our pEV and NonEV proteome datasets (only protein features quantified in <30% of NonEV datasets were used). **b**, A heatmap depicting the quantification of EV protein features in previous reported proteomes for circulating EVs: A–C, EV preparations from plasma or serum sourced from healthy individuals or those with known pathology^{15,69}; D–F, EV subtypes (CD81⁺, CD63⁺ and CD9⁺ EVs) prevalent in the circulatory system⁷⁰. As an orthogonal validation, the heatmap also depicts conservation of EV protein features using TMT-based isobaric multiplexing of pEVs ($n = 4$, independent plasma samples) and in vitro EV proteomes ($n = 6$) (G–J), and using label-free quantitative proteomics for in vitro EVs ($n = 3$ per cell line) (I–L). **c**, A scatter plot of fold change (FDR <0.05) EV protein features and NonEV protein features in the discovery set and validation set (AusDiab set, independent plasma samples). The rest of the proteins are indicated with grey points. Pearson $r = 0.851$, $P < 2 \times 10^{-16}$.

The dotted line represents the linear regression fit (the shaded band indicates the 95% confidence interval, CI). Fold-change correlation between discovery and validation set. Features were first screened by one-way ANOVA (two-sided) on vsn-normalized intensities with Benjamini–Hochberg FDR across features; significant features (FDR <0.05) were analysed using Tukey’s honestly significant difference (HSD) test with Benjamini–Hochberg adjustment applied within each feature. Grey line: least-squares fit with 95% CI band. **d**, Density plot of proteins in pEV proteomes from individuals with either positive CAC score (CAC group) or zero CAC score (Healthy group). CAC_DOWN: proteins significantly (FDR <0.05) downregulated in pEVs from CAC versus Healthy. CAC_UP: proteins significantly (FDR <0.05) upregulated in pEVs from CAC versus Healthy. EV feature: 182 pEV protein features. NS_proteins: proteins with similar abundance between pEVs from CAC versus Healthy.

ITGB1) and annexins (ANXA2 and ANXA5) (Fig. 11 and Supplementary Fig. 6b,c). We further confirmed their surface accessibility in in vitro EVs (Fig. 11 and Supplementary Table 16). By contrast, the conserved SDCBP protein remained inaccessible to biotin capture, which is in direct agreement with its luminal localization³⁰.

By leveraging data from published proteomes^{15,69,70}, we demonstrated a remarkable conservation of pEV protein features in multiple plasma or serum EVs (Fig. 2a,b, A–C, and Supplementary Table 7). These features were also conserved in different EV subpopulations (CD81⁺, CD63⁺ and CD9⁺ EVs) prevalent in the circulatory system (Fig. 2b, D–F),



with 100% quantification of at least 74 proteins. Moreover, interrogating previous published sEV proteomes from 14 cell lines³⁰, 81 EV features were also conserved, displaying greater abundance in EVs compared with cells (Supplementary Fig. 7a,b). In addition, we experimentally verified their conservation in in vitro EVs ($n = 12$) release by four cell lines (Fig. 2b, I–L). Finally, we validated their conservation in pEVs ($n = 4$) and in vitro EVs ($n = 6$) using orthogonal tandem mass tag (TMT)-based isobaric multiplexed proteomics (Fig. 2b, G and H, Supplementary Table 26). Overall, 78 pEV proteins displayed 100% conservation, of which 63 were surface accessible (Supplementary Table 7).

To validate our identified pEV markers, we analysed plasma from an independent external cohort (AusDiab, $n = 12$ pEVs, $n = 12$ NonEVs) using the same EV isolation and proteomic pipeline (Supplementary Table 17). Comparative proteomic analysis revealed that 177 out of 182 pEV protein features and all 42 NonEV protein features were detected, with 87.4% (156/182) of pEV proteins and 92.9% (39/42) of NonEV proteins significantly enriched in their respective fractions (FDR < 0.05) (Supplementary Table 18 and Supplementary Fig. 8), with similar enrichment in Gene Ontology (GO) pathways in our discovery cohort (Supplementary Table 19).

Comparative analysis of fold change of pEV and NonEV protein features between the discovery and validation datasets (Supplementary Table 20) demonstrated a strong positive correlation (Pearson $r = 0.851$, $P < 2 \times 10^{-16}$), confirming the reproducibility of pEV protein features across independent populations (Fig. 2c).

Importantly, we show that pEV protein cargo differs between individuals with and without coronary artery calcium (CAC) deposits in our early detection of coronary artery disease (EDCAD) cohort (Extended Data Fig. 7a–c, Supplementary Tables 21 and 22). The occurrence and development of calcification is a complex biological process that is regulated by multiple factors, including EVs that are regarded as the nidus for calcification by providing mineral nucleation sites⁷¹. CAC scoring, a predictor of future cardiovascular events, is determined by computed tomography. We identified 76 upregulated and 127 downregulated proteins (FDR < 0.05) in pEVs from individuals with positive CAC scores (Extended Data Fig. 7d,e and Supplementary Tables 21 and 22), with the upregulated proteins significantly enriched in the GO pathway ‘Abnormal cardiovascular system physiology’ (Extended Data Fig. 7d and Supplementary Table 23). Notably, this includes Cystatin C (CST3)⁷², TPM2⁷³, TPM1⁷⁴ and TXNRD2⁷⁵, all of which have well-established roles in cardiovascular disease and vascular calcification. Despite these proteomic differences between CAC and non-CAC pEV proteomes, the core set of 182 pEV marker proteins remained highly conserved across both groups (Extended Data Fig. 7f,g and Supplementary Table 24), indicating that the fundamental pEV molecular signature is stable across individuals, potentially even in the context of disease (Fig. 2d). This preservation of core molecular identity in pEVs across CAC and non-CAC individuals, while simultaneously capturing disease-specific molecular shifts in the EDCAD study, reinforces their potential as a well-defined reference for pEV research including disease biomarker discovery. By contrast, NonEV particles and neat plasma proteomes were unable to distinguish CAC from non-CAC individuals, underscoring the power of highly purified pEVs (separated from NonEV particles) in revealing disease-associated changes in the plasma proteome (Supplementary Fig. 9).

To assess the broader biological relevance of pEV protein features beyond plasma-derived EVs, we analysed EV proteomes from non-transformed human fibroblasts and endothelial cells (Extended Data Fig. 8a–d and Supplementary Table 25). Among the 182 pEV protein features, 135 were detected in this dataset, with 43 proteins showing 100% conservation across fibroblast- and endothelial-derived EVs. Conserved proteins included ADAM10, integrins, Rabs, Annexin A5, CD markers (CD9 and CD44) and SDCBP, reinforcing their role as core EV components across different biological sources. Proteins absent from non-transformed cell-derived EVs primarily included immunoglobulins

and complement proteins, supporting their plasma-specific nature or association with the EV protein corona.

Thus, our study defines highly conserved protein features of circulating EVs in human plasma (Table 1 highlights the top 25 EV or NonEV protein features; asterisks indicate surface-accessible proteins).

The lipidome draft of circulating EVs in humans

Next, we defined the lipidome landscape of circulating EVs. The majority of membrane lipids fall under glycosphingolipids, sphingolipids and sterols (predominantly cholesterol (COH) in mammals). Therefore, to capture this lipid diversity, we used a high-throughput targeted-lipidomics platform interrogating 829 lipids representing 40 lipid classes within these three major groups (Fig. 3a, Supplementary Fig. 10 and Supplementary Table 27). Because the lipidomes of small EVs from cells are not as well defined as their proteome counterpart, we also performed lipidome analysis of in vitro EVs and parental cells using the same platform (Supplementary Fig. 10a,b and Supplementary Table 27). We reasoned that circulating EV lipid features should ideally be enriched in in vitro EVs compared with cells.

Principal component analysis (PCA) revealed that pEVs and NonEVs particles (p100K/pDGS.LD) lipidomes were distinct (Fig. 3b). Highly abundant lipids in both pEVs and in vitro EVs included COH, phosphatidylcholine (PC), phosphatidylethanolamine (PE) and sphingomyelin (SM) (Fig. 3c), lipids that are well-recognized major structural components in eukaryotic cell membranes⁷⁶ with housekeeping structural functions. For example, PC forms a planar bilayer with COH, ensuring membrane stability and integrity, while the incorporation of conical PE and SM imposes a curvature stress crucial for membrane budding, fission and fusion. These findings align with previous reports highlighting COH as one of the most abundant EV lipids (40–60% of total lipids)⁷⁷.

Over 30% of measured lipid species displayed differential abundance (adjusted P values < 0.05, fold change > 1.5) between pEVs and NonEVs (p100K/pDGS.LD) (Fig. 3d, Supplementary Fig. 11a,b and Supplementary Table 28). Lipids enriched in pEVs are linked to EV biogenesis⁷⁷ and include dihydroceramides (dhCer)⁷⁸, trihexosylceramides (Hex3Cer) and dihexosylceramides (Hex2Cer) (Supplementary Fig. 11c). These lipids are similarly enriched in in vitro EVs versus their parental cells (Fig. 3d, Supplementary Fig. 11d,e and Supplementary Table 28). By contrast, lipids enriched in NonEVs include the lipid classes COH ester (CE), triacylglycerol (TG) and coenzyme Q10 (CoQ10)⁷⁹, major components of lipoprotein particles. This further supports our EV enrichment pipeline at the lipidomics level.

The core lipidome of circulating EVs

To identify pEV lipid features, we performed K -means clustering of differentially abundant lipids between pEVs versus NonEVs and in vitro EVs versus cells (Fig. 4a and Supplementary Tables 29 and 30), which resulted in four major clusters. Representing pEV lipid features were cluster c4 lipids (52 lipids) enriched in pEVs (compared with NonEVs) and in vitro EVs (compared with cells). By contrast, representing NonEV lipid features were cluster c1 lipids (114 lipids) enriched in NonEVs and cells.

Notably, we observed a class-level coregulation of pEV lipid features (Fig. 4b), supporting previous reports that lipid species from the same pathway correlated/coregulated⁸⁰. For example, lipids from PS and PE class were co-enriched in EVs, which is indicative of their colocalization to external leaflets of EV membranes and coregulating similar cellular processes^{81,82}. Another example includes SM and ceramides co-enriched in EVs, which is indicative of SM–ceramide axis-driven EV biogenesis^{78,83}.

Emphasizing their significance as essential EV lipid components, cluster c4 lipid features (Extended Data Fig. 9) were linked to lipid ontology enrichment analysis (LION) terms such as bilayer membrane and plasma membrane (Fig. 4c), but more specifically with EV features such as glycerophosphatidylserine (known to decorate the outer

Table 1 | List of EV and NonEV protein features

	Gene symbol	Protein name	GO (CC BP)	Reference
EV protein features	ADAM10*	Disintegrin and metalloproteinase domain-containing protein 10	Cell membrane, endomembrane Adherens junction organization	112
	ARPC4*	Actin-related protein 2/3 complex subunit 4	Cell projection, cytoskeleton Actin filament polymerization	113
	CD47*	Leukocyte surface antigen CD47	Cell membrane Integrin-mediated signalling pathway	114
	F11R*	Junctional adhesion molecule A	Cell membrane Actomyosin structure organization	115
	VCP*	Transitional endoplasmic reticulum ATPase	Cytoplasm, ER ER-to-Golgi vesicle-mediated transport	116
	STXBP2	Syntaxin-binding protein 2	Cytosol Vesicle docking involved in exocytosis	117
	RAC1*	Ras-related C3 botulinum toxin substrate 1	Cell membrane (lipid anchor) Actin cytoskeleton organization	118
	ACTR2*	Actin-related protein 2	Cell projection, cytoskeleton Arp2/3 complex-mediated actin nucleation	119
	EHD1*	EH domain-containing protein 1	Early/Recycling endosome Endocytic recycling	120
	FLOT1*	Flotillin-1	Cell membrane, endosome Plasma membrane raft assembly	121
	CAPN1*	Calpain-1 catalytic subunit	Cell membrane, cytoplasm Regulation of catalytic activity	122
	ITGA2*	Integrin alpha-2	Membrane Cell adhesion	123
	NAPA*	Alpha-soluble NSF attachment protein	Peripheral membrane protein Apical protein localization	124
	RAB7A*	Ras-related protein Rab-7a	Lipid anchor, late endosome Endosome to plasma membrane transport	125
	FLOT2	Flotillin-2	Cell membrane, endosome Plasma membrane raft	126
	ARPC3*	Actin-related protein 2/3 complex subunit 3	Cell projection, cytoskeleton Actin polymerization	127
	ARPC2*	Actin-related protein 2/3 complex subunit 2	Cell junction, cell projection Actin filament polymerization	128
	GNA13	Guanine nucleotide-binding protein subunit alpha-13	Membrane (lipid anchor) Rho protein signal transduction	129
	LYN	Tyrosine-protein kinase Lyn	Cell membrane Cell adhesion mediated by integrin	130
	CYFIP1	Cytoplasmic FMR1-interacting protein 1	Cell projection Actin filament polymerization	131
	ACTR3	Actin-related protein 3	Cell projection, cytoskeleton Cell motility	119
	PRKAR1A	cAMP-dependent protein kinase type I-alpha regulatory subunit	Cell membrane G protein-coupled receptor signalling	132
NonEV protein features	SNAP23*	Synaptosomal-associated protein 23	Cell membrane (lipid-anchor) Membrane fusion	133
	PDCD6IP	Programmed cell death 6-interacting protein	Cytoplasm, cytoskeleton Multivesicular body assembly	134
	ANXA11	Annexin A11	Cytoplasm, cytoskeleton Phagocytosis	135
	C6	Complement component C6	Secreted Complement activation	136
	F10	Coagulation factor X	Secreted Blood coagulation	137
	C7	Complement component C7	Secreted Complement activation	138
	CPB2	Carboxypeptidase B2	Secreted Blood coagulation	136
	SERPING1	Plasma protease C1 inhibitor	Secreted Complement activation	139
	F13B	Coagulation factor XIII B chain	Secreted Fibrin clot formation	140
	APOA4	Apolipoprotein A-IV	Secreted Lipid transport	141
	F2	Prothrombin	Secreted Blood coagulation	136
	TF*	Serotransferrin	Secreted Iron ion transport	142
	ORM1*	Alpha-1-acid glycoprotein 1	Secreted Acute-phase response	136
	APOB*	Apolipoprotein B-100	Secreted Lipoprotein transport	136
	SERPINC1	Antithrombin-III	Secreted Blood coagulation	143
	CFI	Complement factor I	Secreted Complement activation	144
	CLEC3B	Tetranectin	Secreted Bone mineralization	145
	AFM	Afamin	Secreted Vitamin transport	146
	AZGP1*	Zinc-alpha-2-glycoprotein	Secreted Immune response	147
	GC*	Vitamin D-binding protein	Secreted Vitamin transport	148
	TTR*	Transthyretin	Secreted Purine nucleobase metabolic process	148
	SERPINA3*	Alpha-1-antichymotrypsin	Secreted Lipid metabolic process	149
	AHSG*	Alpha-2-HS-glycoprotein	Secreted Bone mineralization	145
	HPX	Haemopexin	Secreted Haem metabolic process	150
	A1BG	Alpha-1B-glycoprotein	Secreted	145
	ITIH3	Inter-alpha-trypsin inhibitor heavy chain H3	Secreted Hyaluronan metabolic process	148
	RBP4	Retinol-binding protein 4	Secreted Retinol transport	151
	SERPINF1	Pigment epithelium-derived factor	Secreted Cellular response to retinoic acid	152



Fig. 3 | Lipidome landscape of circulating EVs. **a**, Workflow for lipidomic analysis, interrogating 829 lipids representing 40 lipid classes within three major groups. **b**, PCA of lipidome data showing group clustering and separation of lipidomes (pEVs; $n = 12$, p100K; $n = 6$, pDGS.LD; $n = 5$ (independent plasma samples), in vitro EVs; $n = 12$ (biological replicates), cells; $n = 12$ (3 biological replicates per cell line)). PC, principal component. **c**, Scatter plot depicting the abundance of 829 lipids in pEVs and in vitro EVs with lipids belonging to cluster 3 displaying high abundance in both pEVs and in vitro EVs. **d**, Scatter plot showing the relative abundance of lipids in pEVs versus p100K/pDGS.LD and in vitro EVs versus cell lipidome datasets. Blue circles (lipid markers) represent lipids with

significantly greater abundance (fold change >1.5 and $P < 0.05$). Red circles (exclusion lipids) represent lipids with significantly lower abundance (fold change <-1.5 and $P < 0.05$). Grey circles represent lipids that do not meet the above criteria. Pie chart depicts number of lipids (%) with differential abundance between the datasets. Differential lipid abundance was assessed using a limma-based linear-model framework with empirical-Bayes moderation applied to vsn-normalized intensities. Two-sided moderated t -tests were used for pairwise contrasts. Multiple-testing-adjusted q values (Benjamini–Hochberg FDR) are reported in Supplementary Table 28.

membrane/leaflet of EVs) and low lateral diffusion (a distinct physical property of lipid rafts⁸⁴ that are hubs for EV formation). Conversely, cluster c1 NonEV lipid features (Extended Data Fig. 9) were associated with lipid storage and droplets, characteristic of lipoprotein particles.

To validate the association of cluster c4 lipids with circulating EVs, and cluster c1 with NonEV particles in plasma, we subjected 12 fractions of plasma DGS ($n = 3$ plasma samples) to the same targeted lipidomics platform (Fig. 4d,e, Supplementary Fig. 12a,b and Supplementary Tables 30 and 31). The normalized abundance of lipids across the fractions was plotted (z-scored within each fraction) (Fig. 4f). Indeed, cluster c4 lipids were enriched in DGS fractions 6 and 7, where pEVs resolve. By contrast, cluster c1 lipids were enriched in DGS fractions 1–4, where the majority of NonEV particles resolve, reinforcing the specificity of cluster c4 lipids for circulating EVs in plasma.

To further assess the conservation of pEV lipid features, we performed lipidomic profiling of pEVs and NonEVs isolated from two sets of plasma from AusDiab study ($n = 10$ plasma samples for validation set 1 and $n = 12$ plasma samples for validation set 2) and non-transformed (primary human fibroblasts and endothelial cells) cell-derived EVs (Extended Data Fig. 10a,b, Supplementary Table 32 and Supplementary Fig. 13). In this validation lipidomic workflow, we requantified 12 out of 52 pEV lipid features and 48 out of 114 NonEV lipid features and report their differential abundance analysis (Supplementary Tables 32 and 33 and Supplementary Fig. 14). Comparison of fold changes between these lipid features across the discovery and validation datasets showed a strong correlation (Fig. 4g and Supplementary Table 34, Pearson $r = 0.901$, $P < 2 \times 10^{-16}$ for validation set 1, and Pearson $r = 0.878$, $P < 2 \times 10^{-16}$ for validation set 2), confirming the reproducibility of pEV lipid features. The relative abundance of these features was also conserved in EVs from primary human fibroblasts and endothelial cells (Extended Data Fig. 10b and Supplementary Fig. 14). These findings highlight the robustness of our identified EV lipid markers across independent populations and multiple EV sources.

Thus, our study defines highly conserved lipid features of circulating EVs in human plasma (Table 2; asterisks indicate the top 25 enriched lipids in either pEVs or NonEVs, based on relative fold change in abundance).

Biological protein and lipid markers for circulating EVs

We next investigated the ability of the EV and NonEV protein feature panel to distinguish between pEVs versus NonEV particles using

machine learning (naive Bayes algorithm). For this, pEV and NonEV proteomes were evenly partitioned on the basis of sample type into a training set (70% of the samples) and a validation set (remaining 30% of samples). By the bootstrapping resampling method using 25 resampling iterations, the model achieved absolute accuracy (Supplementary Fig. 15a). Our model also achieved excellent accuracy (97%) in EV particle identification in an independent test set comprising of pEVs and NonEVs proteomes from additional 16 plasma samples (Supplementary Fig. 15a). Moreover, a panel comprising 151 surface-accessible EV protein features was also able to distinguish between EV and NonEV particles with 100% accuracy (Supplementary Fig. 15b).

To facilitate routine implementation and translational feasibility, we applied recursive feature elimination (RFE) to systematically reduce dimensionality and identify a robust minimal signature with classification accuracy. Among the 182 EV protein features, the RFE-based random forest algorithm identified ADAM10 as a prominent feature contributing to model performance (Supplementary Table 35). Moreover, ADAM10 protein showed exclusive and absolute quantification in pEVs as well as in vitro EVs, compared with NonEVs (Fig. 5a). Moreover, within each EV proteome the abundance of ADAM10 was up to 7.5-fold higher compared with the median intensity (Fig. 5b and Supplementary Table 36); this relative abundance of ADAM10 within each proteome alone can distinguish between pEVs versus NonEV particles (Supplementary Fig. 15c).

Similarly, using a neural network algorithm ('nnet') for machine learning, a panel comprising EV and NonEV lipid features was also able to distinguish between EVs (pEVs or in vitro EV lipidomes) and NonEVs (p100K, pDGS.LD or cell lipidomes) (Supplementary Fig. 16a). Moreover, this model achieved 97% accuracy in classifying EV particles across DGS plasma fractions (Supplementary Fig. 16b).

To enhance translational feasibility, we applied RFE to reduce dimensionality and identify a minimal lipid signature with high classification accuracy. This approach identified PS(36:1) (EV lipid feature) and CE(18:0) as prominent lipid features (Supplementary Table 35), highlighting their marker potential.

Indeed, PS(36:1) lipid is one of the most abundant lipids present in both pEVs and in vitro EVs (Figs. 3c and 5c), making them amenable to robust and reliable measurements in diverse analytic tools. Moreover, PS(36:1) and CE(18:0) lipid abundances, and importantly their relative abundances, concur with EV protein CD63 and lipoprotein APOB100

Fig. 4 | Conserved lipid features of circulating EVs in humans. **a**, Heatmap depicting K -means clustering of differentially abundant lipids from **d**. **b**, Network map of lipids grouped based on lipid classes. Blue circles represent EV-associated lipid clusters c2, c3 and c4, whereas red circles represent NonEV-associated lipid cluster c1. Grey circles are lipids with similar abundance between EVs and NonEVs. **c**, LION Ontologies enriched in EV lipid features (cluster c4 lipids) or NonEV lipid features (cluster c1 lipids). The circle size indicates the number of lipids in EVs or NonEVs involved in each term. **d**, DGS of plasma. The 12 fractions were subjected to lipidomics analysis. **e**, PCA of lipidomes of 12 fractions ($n = 3$, independent plasma samples). **f**, Box plots depict abundance of cluster 1–4 lipids for DGS fractions ($n = 3$, DGS experiments using independent plasma samples). The Y axis represents Z-scored abundance (MS-based abundance for each lipid - mean abundance)/standard deviation (z-score normalization). Grey lines mark either fractions 6–7 (corresponding to pEV fractions) or fractions 1–3

(corresponding to pDGS.LD fractions). Lipids from cluster c4 and cluster c1 are depicted. The boxplot displays the median (centre line), 25th–75th percentiles (box) and the minimum and maximum values within $1.5 \times$ the interquartile range (whiskers); individual data points are overlaid. **g**, Scatter plot of fold change (FDR < 0.05) EV lipid features and NonEV lipid features in the discovery set and two validation sets (AusDiab set). The rest of the lipids are indicated with grey points. Fold-change correlation between discovery and validation sets. Features were first screened by one-way ANOVA (two-sided) on vsn-normalized intensities with Benjamini–Hochberg FDR across features; significant features (FDR < 0.05) were subjected to Tukey's HSD test with Benjamini–Hochberg adjustment applied within each feature. Points highlight features significant as EV (blue) or NonEV (red) in both sets. Grey line: least-squares fit with 95% CI band. $P = 2.673044 \times 10^{-22}$ (validation set 1) and $P = 6.562873 \times 10^{-20}$ (validation set 2).

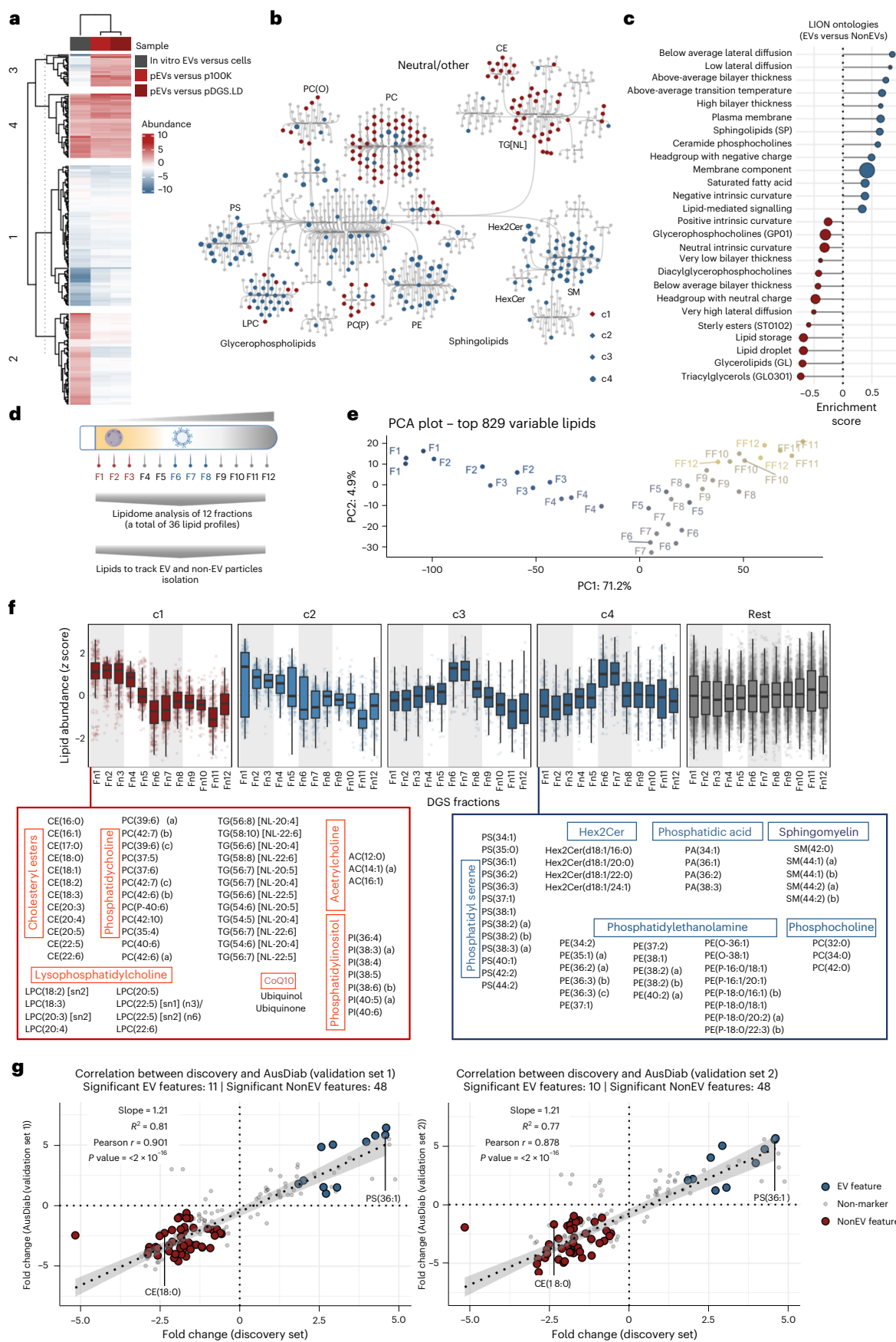


Table 2 | List of EV and NonEV lipid features

	Class	Lipids	Number	Description	References
EV lipid features	PA	PA(34:1)*, PA(36:1)*, PA(36:2)*, PA(38:3)*	4	Phosphatidic acid (PA): involved in cell signalling, membrane trafficking and lipid metabolism.	153,154
	PC	PC(32:0), PC(34:0), PC(42:0)	4	PC: major component of cell membranes, critical for membrane structure and function.	155,156
	PE	PE(35:1) (a)*, PE(36:2) (a)*, PE(38:2) (a)*, PE(38:2) (b)*, PE(40:2) (a)*	11	PE: another major membrane phospholipid, essential for membrane integrity and cellular processes.	157
	PE(O)	PE(O-36:1), PE(O-38:1)	2	Alkylphosphatidylethanolamine (PE(O)): ether lipid class that is synthesized in a peroxisomal-dependent pathway.	158
	PE(P)	PE(P-18:0/16:1) (b)*, PE(P-18:0/20:2) (a)*, PE(P-18:0/22:3) (b)*	6	PE plasmalogen (PE(P)): also involved in membrane structure and antioxidant defence.	157
	PS	PS(34:1)*, PS(36:1)*, PS(36:2)*, PS(36:3)*, PS(37:1)*, PS(38:1)*, PS(38:2) (a)*, PS(38:2) (b)*, PS(38:3) (a)*, PS(40:1)*	13	Phosphatidylserine (PS): plays roles in cell signalling, apoptosis and blood clotting. Enriched in platelets and EVs.	159,160
	Hex2Cer	Hex2Cer(d18:1/20:0)*, Hex2Cer(d18:1/22:0)*, Hex2Cer(d18:1/24:1)*	4	Hex2Cer: a glycosphingolipid involved in cell signalling and membrane dynamics.	161
	SM	SM(42:0), SM(44:1) (a), SM(44:2) (a), SM(44:2) (b)	5	SM: another glycosphingolipid, important for membrane structure and stability.	162,163
NonEV lipid features	AC	AC(12:0), AC(14:1) (a)*, AC(16:1)	3	Acylcarnitine (AC): involved in fatty acid transport and mitochondrial energy metabolism.	164
	CE	CE(18:0)*, CE(18:2)*, CE(18:3)*, CE(20:3)*, CE(20:4)*, CE(20:5)*, CE(22:5)*, CE(22:6)*	12	Cholesteryl ester (CE): form of COH storage, found in lipid droplets and lipoprotein particles.	165
	LPC	LPC(18:2) [sn2]*, LPC(18:3)*, LPC(20:4)*, LPC(20:5)*	7	Lysophosphatidylcholine (LPC): implicated in inflammation, endothelial dysfunction and lipid metabolism.	166
	PC	PC(37:5)*, PC(37:6)*, PC(39:6) (a)*, PC(39:6) (c)*, PC(42:7) (b)*, PC(42:7) (c)*	43	PC: major component of cell membranes, essential for membrane structure and function.	167
	PC(O)	PC(O-36:4), PC(O-38:4) (b), PC(O-38:6) (b)	6	Alkylphosphatidylcholine (PC(O)): ether lipid class that is synthesized in a peroxisomal-dependent pathway.	168,169
	PC(P)	PC(P-36:4), PC(P-38:3), PC(P-38:6), PC(P-42:5)	9	PC plasmalogen (PC(P)): also involved in membrane structure and antioxidant defence.	170,171
	PI	PI(38:3) (a)*, PI(38:6) (b)*, PI(40:5) (a), PI(40:6)*	7	Phosphatidylinositol (PI): important for cell signalling, membrane trafficking, and cytoskeletal dynamics.	172
	TG[NL]	TG(52:3) [NL-18:2], TG(56:7) [NL-20:4], TG(56:8) [NL-20:4]*, TG(58:10) [NL-22:6]*	24	Triglycerides (TG[NL]): main storage form of fats in the body, core component of lipid droplets, serving as an energy reservoir.	173
	CoQ10	Ubiquinol*, Ubiquinone	2	CoQ10: essential for cellular energy production, antioxidant activity and mitochondrial function.	174

resolution on plasma DGS fractions (Fig. 5d,e). Our machine learning ('nnet') model, based on PS(36:1) and CE(18:0) relative abundance within each lipidome serving as a feature (Supplementary Table 37), can distinguish EVs (pEVs or in vitro EV, DGS fraction 6–7 lipidomes) versus NonEVs (p100K, pDGS.LD or DGS fraction 1–5 lipidomes) with absolute accuracy (Fig. 5f). Because EV and NonEV enrichments along 12 fractions represent a continuum, which can be inferred from PS(36:1) and CE(18:0) relative abundances, our data suggest that these lipids can serve as a marker for assessment of EV purity. Importantly, quantitative measurement would be possible in subsequent studies owing to the availability of isotope-labelled internal standards for these two species, which assist in translation across different laboratories and instrumental setups.

We next investigated whether PS and ADAM10 constitute protein and lipid biological marker componentry on circulating EVs. For this, we used a previously reported⁸⁵ strategy of using an extracellular region of the T cell immunoglobulin domain and mucin domain-containing protein 4 (Tim4) immobilized on magnetic beads to directly capture (in the presence of calcium ions) PS⁺ EVs from plasma ($n = 23$), which was subsequently released (by adding EDTA) and subjected to MS proteomics (Fig. 5g and Supplementary Table 38). Compared with mock capture (beads alone) or unprocessed plasma, PS⁺ EV proteomes displayed 100% quantification of ADAM10 across all 23 samples (Fig. 5g).

Additional EV protein features (for example, FLOT2 and RAB7A) were also conserved in these proteomes, which support their EV identity.

Furthermore, single-vesicle analysis using Cytek Aurora flow cytometry confirmed the presence of ADAM10 on a subset of pEVs (Fig. 5h and Supplementary Fig. 17), with ~40% of pEVs exhibiting ADAM10⁺ signals, comparable to PS signal detected using Annexin V staining (Fig. 5h, Supplementary Fig. 17c and Supplementary Table 39). Sodium dodecyl sulfate (SDS) detergent treatment showed a strong reduction in fluorescence signal intensity and count, suggesting their EV origin⁸⁶ (Supplementary Figure 17b,c). These findings suggest that, while ADAM10 is a component of pEVs across individuals, it is not universally present across all vesicles, consistent with a previous report⁸⁷.

In our validation set, PS(36:1) lipid was significantly enriched in pEVs and in vitro EVs, reinforcing its role as a conserved pEV lipid marker (Extended Data Fig. 10c). By contrast, CE(18:0) lipid was enriched in NonEVs and neat plasma (Extended Data Fig. 10c). These findings confirm that pEV protein and lipid markers are conserved beyond plasma-derived EVs, reinforcing their biological significance and potential as robust EV classification markers.

Thus, our data show that ADAM10 and the ratio combination of PS(36:1) and CE(18:0) serve as highly conserved and reliable biological markers for EVs in human plasma.

R/Shiny web tool for EV proteome and lipidome data

Lastly, to facilitate easy access to our data and enhance reuse, we have developed an open-source R/Shiny web tool (evmap.shinyapps.io/evmap/). This tool allows users to quickly interrogate our proteome (Fig. 6a,b and Supplementary Fig. 18) and lipidome datasets (Fig. 6a,b and Supplementary Fig. 19) for their molecule(s) of interest. This tool also allows the assessment of feature conservation in published studies, analysis of surface accessibility of EV proteins, construction of network analyses, and retrieval of GO and KEGG pathways for selected protein features. Lipid features can also be quickly interrogated for their abundance in EVs versus NonEV particles and their distribution in plasma DGS lipidome fractions. We anticipate that this tool will enable broad utilization of our data and will serve as a valuable repository for the broader EV community.

Discussion

In our study, we integrated multi-omics investigation to systematically resolve the core protein and lipid componentry of circulating EVs in humans (Fig. 6a). Our discovery includes a conserved set of 182 proteins and 52 lipids intrinsic to circulating EVs, and a panel of 29 proteins and 114 lipids that are NonEV features in plasma, which together serve as biological markers for EV research applicable to human samples. As a resource, these extensive protein and lipid landscapes, which can be easily accessed with the Shiny web tool (Fig. 6b), will be instrumental to the EV community in advancing a clearer understanding of circulating EV biology. This includes the survey of circulating EV surfaceome, comprising 151 EV protein features, that could be exploited for antibody-based capture of circulating EVs based on their surface protein expression(s). In addition to this resource, we identified a minimal set of biomarkers—ADAM10 (protein), PS(36:1) and CE(18:0) (lipids)—with strong discriminatory power between EVs and NonEVs. This reduced marker set is compatible with targeted, scalable assays such as enzyme-linked immunosorbent assay or targeted MS, making it highly practical for clinical translation. Furthermore, the ranked feature list generated by our machine learning framework provides a valuable resource for the research community, enabling prioritization of alternative markers based on available reagents or disease-specific applications.

The highly conserved protein ADAM10 on circulating EVs is also included in this EV surfaceome. The role of ADAM10 as a conserved and robust EV marker is further supported by various studies reporting its expression in circulating EVs from human plasma, other biofluids and EVs released by diverse tissue and cell types, using a range of biochemical analyses and EV isolation strategies. Moreover, ADAM10 was also highly conserved in different circulating EV subpopulations (based on surface expression of tetraspanins, CD9, CD63 and CD81⁷⁰). The surface localization of ADAM10 is also corroborated in previous reports⁸⁸. Conversely, the EV lipid feature PS¹⁵ has already been leveraged for

capturing circulating EVs using TIM4-based magnetic beads. The selective presence of ADAM10 (and PS lipids) in only a subset of EVs highlights the non-random nature of EV cargo packaging, supporting models of regulated biogenesis pathways such as endosomal sorting complexes required for transport (ESCRT)-dependent sorting⁸⁹. Evidence that ADAM10 retains proteolytic activity in EVs⁹⁰ suggests that these vesicles may serve as active mediators of extracellular remodelling and intercellular communication, expanding their functional relevance beyond passive biomarker carriers. The differential association of ADAM10 with specific EV subtypes, and its absence from some canonical small EV populations⁸⁷, underscores the existence of biophysically and functionally distinct EV in circulation. Together, these findings support a growing consensus that EV heterogeneity is biologically regulated rather than stochastic, with specific protein profiles reflecting distinct functional roles in physiological and pathological contexts^{87,89,90}.

Our data also provide 'high-confidence' molecular leads for studying EV biology in multimodal organisms, particularly targeting EV biogenesis to curb EV-driven pathogenesis in complex organisms such as the mouse⁸³, a model that remains largely unexplored. For instance, EV protein feature STEAP3 (also known as TSAP6) has been shown to regulate EV biogenesis in mice⁹¹. A holistic analysis of the core protein and lipid componentry can also provide insights into biological pathways co-involved in proteins and lipids; one such biology includes the potential involvement of lipid raft biology in human EVs. For instance, EV features such as flotillins⁹², SM and PS, along with COH (the most abundant lipids in EVs), are core components of lipid raft domains⁸⁴. Assembly of flotillins in SM/ceramide⁸⁴-rich microdomains induces curvature stress⁹³ to regulate EV biogenesis and cargo selection^{78,94} in ESCRT⁹⁵ and syntenin/syndecan-independent mechanisms⁹⁶. Moreover, proteins that constitute the cortical actin—identified as an enriched KEGG term among EV core proteins—help maintain and remodel these domains⁸⁴. Accumulating evidence suggests that lipid rafts serve as a nidus for EV biogenesis and are present in EVs as functional units⁹⁴. Moreover, several bioactive cargo quantified in pEVs—such as TGFβ1⁶⁶, the RNA-binding protein HNRNPK⁶², integrins⁵⁷ and SRC kinases⁶⁵—are closely linked to lipid raft assembly and trafficking^{97–100}. Importantly, classical lipid-raft-modulating proteins such as CAV1 and CAVIN1—known to regulate membrane microdomain composition and influence the EV proteome^{101,102}—regulate microRNA cargo loading into EVs by modulating HNRNPK within the membrane raft⁶². Elevated levels of EV-associated HNRNPK have also been detected in body fluids from patients with metastatic prostate and colorectal cancers, underscoring its clinical relevance. Ubiquitous identification of these features in pEVs highlights similar EV biogenesis and cargo sorting mechanisms conserved for circulating EVs in humans.

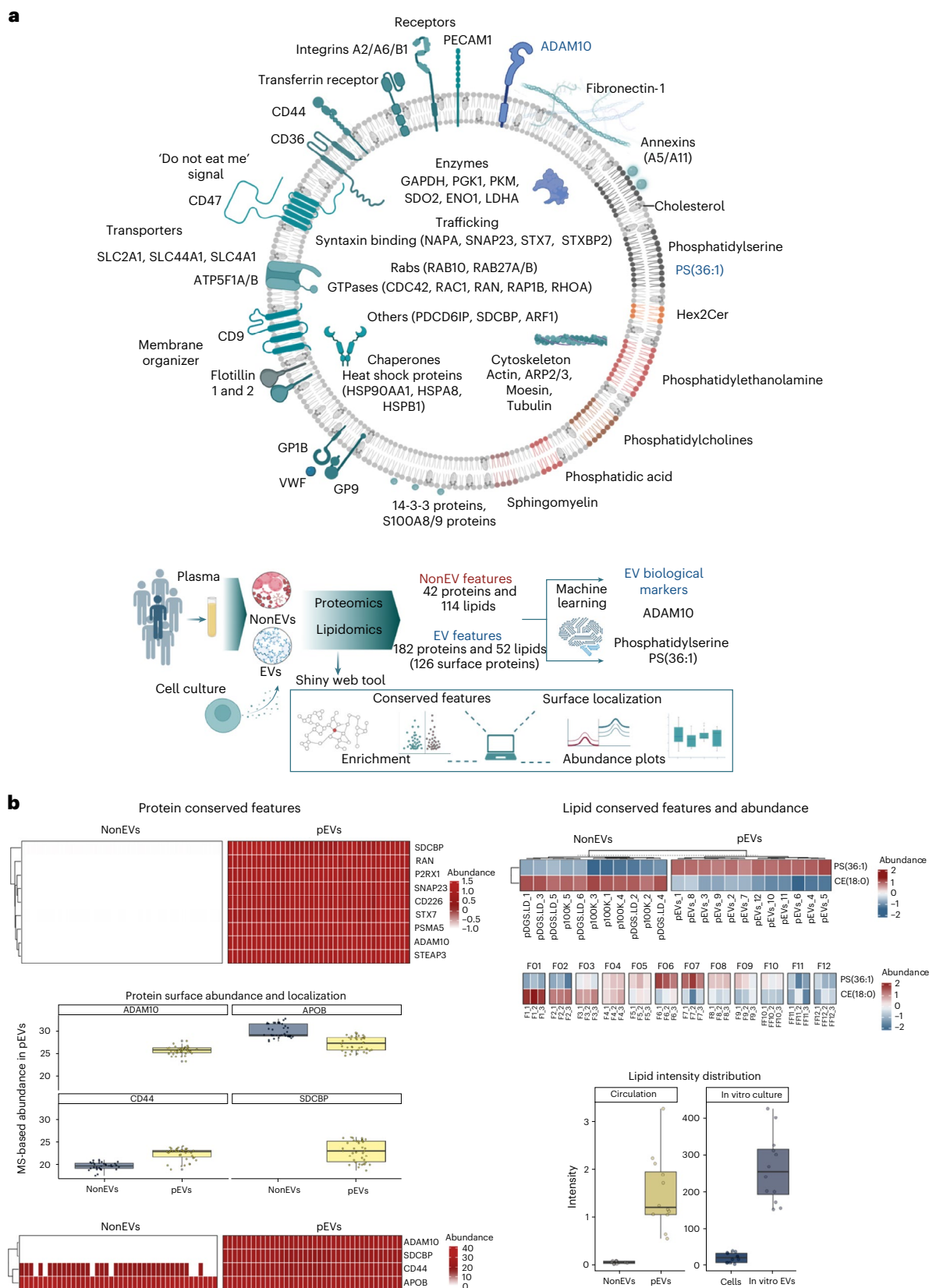
A major caveat in our study is that it primarily focuses on bulk preparation of small EVs present in human plasma. Cells release

Fig. 5 | ADAM10 protein and phosphatidylserine lipid are biological markers for circulating EVs in humans. a, Heatmap depicting pEV protein features that are uniquely identified in pEVs compared with NonEVs and their conservation, in particular for ADAM10, in previously published circulating EV proteomes^{15,69}

(A–C) and EV subtypes (CD81⁺, CD63⁺ and CD9⁺ EVs) in plasma (D–F)⁷⁰, and in our TMT-based isobaric multiplexing of pEVs ($n = 4$, independent plasma samples) and in vitro EVs proteomes ($n = 6$, biological replicates) as well as label-free proteomes of small EVs from 4 cell lines ($n = 3$, biological replicates, per cell line) and pEV proteome ($n = 38$, independent plasma samples) (I–L). b, The ratio of ADAM10 intensity and corresponding sample median intensity for each proteome, depicted as a boxplot. The boxplot shows the median (centre line), 25th–75th percentiles (box) and minima and maxima within 1.5× interquartile range (whiskers); individual data points are overlaid. c, Box plot depicting normalized intensities (abundance log₂-transformed) and raw intensities of PS(36:1) and CE(18:0) in indicated lipidome datasets (NonEV $n = 11$, pEV $n = 12$; independent plasma samples). Boxplot shows the median (centre line), 25th–75th percentiles (box) and minima and maxima within 1.5× interquartile range (whiskers); individual data points are overlaid. d, The abundance of PS(36:1)

and CE(18:0) in lipidome datasets across 12 DGS fractions ($n = 3$, independent plasma samples). Grey points represent the rest of the quantified lipids. e, Top: the relative abundance of PS(36:1) and CE(18:0) in lipidome datasets across 12 DGS fractions ($n = 3$, independent plasma samples). Middle: the median of lipidome datasets across 12 DGS fractions. Bottom: western blot analysis of 12 fractions for indicated proteins. Boxplot shows the median (centre line), 25th–75th percentiles (box) and minima and maxima within 1.5× interquartile range (whiskers); individual data points are overlaid. f, Confusion matrix using the neural network algorithm ('nnet') classifier of the training set (70%) and validation set (30%) using the relative abundance of PS(36:1) versus CE(18:0). g, The workflow for capturing PS⁺ EVs from human plasma using TIM4-magnetic bead conjugate. Captured EVs ($n = 23$, independent plasma samples), along with mock capture using beads alone ($n = 3$, independent plasma samples) or unprocessed plasma ($n = 3$, independent plasma samples), were subjected to proteomics analysis. The heatmap depicts absolute and exclusive quantification of ADAM10 protein in captured EVs. h, Scatter plot showing the detection of ADAM10-positive and PS-positive pEVs, which was sensitive to SDS detergent (0.5%) solubilization.





and serve as a valuable repository to the research community for a clearer understanding of circulating EV biology. Boxplot show the median (centre line), 25th--75th percentiles (box) and minima and maxima within 1.5× interquartile range (whiskers); individual data points are overlaid. Panel **a** was created with [BioRender.com](https://www.biorender.com/).

heterogeneous EV populations^{36,45,103,104} that display functional diversity¹⁰⁵. They can be categorized on the basis of their origin^{45,106,107}, density^{45,50,104}, biochemical composition^{31,50} and size^{47,50}. Because current EV isolation strategies cannot purify a specific subset of EVs to homogeneity, operational terms such as small EVs (30–150 nm) and large EVs (100–1,000 nm) are encouraged where evidence for subcellular origin cannot be ascertained. In our study, small EVs potentially include both exosomes (endosomal-derived) and microvesicles (shed from plasma membrane) evident from our EV protein markers that include markers of both EV subtype (TSG101 and ANXA2). Thus, our EV markers are applicable in a broad sense to small EVs; their specificity in exosomes versus microvesicles can potentially provide greater resolution in human EV biology and thus warrants future investigation. Moreover, EV heterogeneity is reported in circulating EVs too based on surface expression of tetraspanins, CD9, CD63 and CD81⁷⁰. Nonetheless, our EV protein features show high conservation in all three EV subpopulations⁷⁰. While bulk EV study provides a broader understanding of the complex interactions and processes involving EVs within the body that specific EV subtypes might not fully capture, it is essential to study EV subpopulation-specific core features in humans, as this avenue holds great potential for advancing precise diagnostics and therapeutics. Nevertheless, bulk analyses can still offer insights into coordinated molecular patterns and biologically conserved pathways. For instance, enrichment patterns observed in our study (Extended Data Fig. 6) reflects functionally associated protein modules enriched in the pEV pool. While these associations do not imply direct molecular interactions or spatial colocalization within individual EVs, they highlight coordinated expression patterns that are recurrent across EV subtypes and cell types. Importantly, we validated that many of these molecular features are enriched in EVs derived from multiple cell types—including cancer cells and primary fibroblasts—as well as across CD9-, CD63- and CD81-positive pEVs, suggesting they are not artefacts of averaging but representative of fundamental EV-associated signatures. Our findings align with prior studies demonstrating that such molecules are actively enriched in EVs relative to their cells of origin and conserved across cell-derived EVs³⁰. Thus, while single-vesicle resolution would offer even deeper insight, bulk EV analysis can still uncover biologically meaningful and source-representative features that contribute to systemic intercellular communication. In regard to source attribution, protein signatures associated with diverse cell types were represented in pEVs, including endothelial cells, fibroblasts, hepatocytes, cardiomyocytes, kidney cells and haematopoietic cells (such as platelets), corroborating previous reports^{15,54,55,108,109}. In healthy individuals, circulating EVs reportedly arise from haematopoietic cells (such as platelets, erythrocytes and leukocytes) and endothelial cells^{54,55}. While definitive source attribution of pEVs remains technically challenging due to the lack of universally exclusive surface markers, recent computational deconvolution algorithms offer promising solutions to estimate the relative contribution of different cell types^{108,109}. Complementary proteomic studies have also identified tissue-specific EV-associated proteins, providing valuable leads for understanding EV origin and function in systemic circulation¹⁵. In parallel, high-sensitivity techniques such as single-vesicle flow cytometry and antibody-based surface profiling^{110,111} offer additional means to enrich and classify EVs on the basis of cellular source, which may be used alongside our reference EV proteome dataset to further refine classification and improve translational application. Our dataset offers a high-confidence resource of tissue- and cell-enriched protein features in circulating EVs that can be harnessed to guide the development of affinity-based enrichment strategies, improve computational deconvolution models and support source-specific EV biomarker discovery. In future studies, combining these molecular leads with advanced single-EV technologies and disease-specific profiling could yield deeper insights into tissue-specific EV biogenesis, intercellular communication and their roles in health and disease. Importantly, despite disease-associated proteomic changes, the core

set of 182 pEV protein features remained highly conserved across both CAC and non-CAC individuals in the EDCAD cohort, underscoring their robustness as molecular hallmarks of circulating EVs. This warrants future investigation on molecular stability across diverse disease states to establish the use of these core pEV features as a reliable foundation for human pEV studies in large population-based cohorts, enabling consistent characterization and cross-study comparability.

In summary, we identify core protein and lipid componentry of circulating EVs in humans. We propose these as ‘hallmark molecular features’ of circulating EVs, offering a valuable resource to the EV community and a tool to enhance the quality of human EV research.

Online content

Any methods, additional references, Nature Portfolio reporting summaries, source data, extended data, supplementary information, acknowledgements, peer review information; details of author contributions and competing interests; and statements of data and code availability are available at <https://doi.org/10.1038/s41556-025-01795-7>.

References

- Xu, R. et al. Extracellular vesicles in cancer—implications for future improvements in cancer care. *Nat. Rev. Clin. Oncol.* **15**, 617–638 (2018).
- van Niel, G., D’Angelo, G. & Raposo, G. Shedding light on the cell biology of extracellular vesicles. *Nat. Rev. Mol. Cell Biol.* **19**, 213–228 (2018).
- Dixon, A. C., Dawson, T. R., Di Vizio, D. & Weaver, A. M. Context-specific regulation of extracellular vesicle biogenesis and cargo selection. *Nat. Rev. Mol. Cell Biol.* **24**, 454–476 (2023).
- Valadi, H. et al. Exosome-mediated transfer of mRNAs and microRNAs is a novel mechanism of genetic exchange between cells. *Nat. Cell Biol.* **9**, 654–659 (2007).
- Skog, J. et al. Glioblastoma microvesicles transport RNA and proteins that promote tumour growth and provide diagnostic biomarkers. *Nat. Cell Biol.* **10**, 1470–1476 (2008).
- Peinado, H. et al. Melanoma exosomes educate bone marrow progenitor cells toward a pro-metastatic phenotype through MET. *Nat. Med.* **18**, 883–891 (2012).
- Iannotta, D., A., A., Kijas, A. W., Rowan, A. E. & Wolfram, J. Entry and exit of extracellular vesicles to and from the blood circulation. *Nat. Nanotechnol.* **19**, 13–20 (2023).
- Yuana, Y. et al. Cryo-electron microscopy of extracellular vesicles in fresh plasma. *J. Extracell. Vesicles* **2**, 21494 (2013).
- Arraud, N. et al. Extracellular vesicles from blood plasma: determination of their morphology, size, phenotype and concentration. *J. Thromb. Haemost.* **12**, 614–627 (2014).
- Karimi, N. et al. Detailed analysis of the plasma extracellular vesicle proteome after separation from lipoproteins. *Cell. Mol. Life Sci.* **75**, 2873–2886 (2018).
- Andaluz Aguilar, H., Iliuk, A. B., Chen, I. H. & Tao, W. A. Sequential phosphoproteomics and N-glycoproteomics of plasma-derived extracellular vesicles. *Nat. Protoc.* **15**, 161–180 (2020).
- Dong, L. et al. Comprehensive evaluation of methods for small extracellular vesicles separation from human plasma, urine and cell culture medium. *J. Extracell. Vesicles* **10**, e12044 (2020).
- Toth, E. A. et al. Formation of a protein corona on the surface of extracellular vesicles in blood plasma. *J. Extracell. Vesicles* **10**, e12140 (2021).
- Veerman, R. E. et al. Molecular evaluation of five different isolation methods for extracellular vesicles reveals different clinical applicability and subcellular origin. *J. Extracell. Vesicles* **10**, e12128 (2021).
- Muraoka, S. et al. Comprehensive proteomic profiling of plasma and serum phosphatidylserine-positive extracellular vesicles reveals tissue-specific proteins. *iScience* **25**, 104012 (2022).

16. Adamczyk, A. M. et al. Extracellular vesicles from human plasma dampen inflammation and promote tissue repair functions in macrophages. *J. Extracell. Vesicles* **12**, e12331 (2023).
17. Wang, J. et al. Extracellular vesicles mediate the communication of adipose tissue with brain and promote cognitive impairment associated with insulin resistance. *Cell Metab.* **34**, 1264–1279 (2022).
18. Ying, W. et al. Adipose tissue macrophage-derived exosomal miRNAs can modulate in vivo and in vitro insulin sensitivity. *Cell* **171**, 372–384 (2017).
19. Sahu, A. et al. Regulation of aged skeletal muscle regeneration by circulating extracellular vesicles. *Nat. Aging* **1**, 1148–1161 (2021).
20. Viegas, C. S. B. et al. Chronic kidney disease circulating calciprotein particles and extracellular vesicles promote vascular calcification: a role for GRP (Gla-rich protein). *Arterioscler Thromb. Vasc. Biol.* **38**, 575–587 (2018).
21. Safdar, A., Saleem, A. & Tarnopolsky, M. A. The potential of endurance exercise-derived exosomes to treat metabolic diseases. *Nat. Rev. Endocrinol.* **12**, 504–517 (2016).
22. Deatherage, B. L. & Cookson, B. T. Membrane vesicle release in bacteria, eukaryotes, and archaea: a conserved yet underappreciated aspect of microbial life. *Infect. Immun.* **80**, 1948–1957 (2012).
23. Hoshino, A. et al. Extracellular vesicle and particle biomarkers define multiple human cancers. *Cell* **182**, 1044–1061 e18 (2020).
24. Zhou, R., Bozbas, E., Allen-Redpath, K. & Yaqoob, P. Circulating extracellular vesicles are strongly associated with cardiovascular risk markers. *Front. Cardiovasc. Med.* **9**, 907457 (2022).
25. Lam, S. M. et al. A multi-omics investigation of the composition and function of extracellular vesicles along the temporal trajectory of COVID-19. *Nat. Metab.* **3**, 909–922 (2021).
26. Shao, H. et al. Protein typing of circulating microvesicles allows real-time monitoring of glioblastoma therapy. *Nat. Med.* **18**, 1835–1840 (2012).
27. Rai, A., Claridge, B., Lozano, J. & Greening, D. W. The discovery of extracellular vesicles and their emergence as a next-generation therapy. *Circ. Res.* **135**, 198–221 (2024).
28. Welsh, J. A. et al. Minimal information for studies of extracellular vesicles (MISEV2023): from basic to advanced approaches. *J. Extracell. Vesicles* **13**, e12404 (2024).
29. Kim, M. S. et al. A draft map of the human proteome. *Nature* **509**, 575–581 (2014).
30. Kugeratski, F. G. et al. Quantitative proteomics identifies the core proteome of exosomes with syntenin-1 as the highest abundant protein and a putative universal biomarker. *Nat. Cell Biol.* **23**, 631–641 (2021).
31. Jeppesen, D. K. et al. Reassessment of exosome composition. *Cell* **177**, 428–445 e18 (2019).
32. Takov, K., Yellon, D. M. & Davidson, S. M. Comparison of small extracellular vesicles isolated from plasma by ultracentrifugation or size-exclusion chromatography: yield, purity and functional potential. *J. Extracell. Vesicles* **8**, 1560809 (2019).
33. Baranyai, T. et al. Isolation of exosomes from blood plasma: qualitative and quantitative comparison of ultracentrifugation and size exclusion chromatography methods. *PLoS ONE* **10**, e0145686 (2015).
34. Sodar, B. W. et al. Low-density lipoprotein mimics blood plasma-derived exosomes and microvesicles during isolation and detection. *Sci. Rep.* **6**, 24316 (2016).
35. Yuana, Y., Levels, J., Grootemaat, A., Sturk, A. & Nieuwland, R. Co-isolation of extracellular vesicles and high-density lipoproteins using density gradient ultracentrifugation. *J. Extracell. Vesicles* **3**, 23262 (2014).
36. Thery, C. et al. Minimal information for studies of extracellular vesicles 2018 (MISEV2018): a position statement of the International Society for Extracellular Vesicles and update of the MISEV2014 guidelines. *J. Extracell. Vesicles* **7**, 1535750 (2018).
37. Vergauwen, G. et al. Robust sequential biophysical fractionation of blood plasma to study variations in the biomolecular landscape of systemically circulating extracellular vesicles across clinical conditions. *J. Extracell. Vesicles* **10**, e12122 (2021).
38. Thippabhotla, S., Zhong, C. & He, M. 3D cell culture stimulates the secretion of in vivo like extracellular vesicles. *Sci. Rep.* **9**, 13012 (2019).
39. Rocha, S. et al. 3D cellular architecture affects MicroRNA and protein cargo of extracellular vesicles. *Adv. Sci.* **6**, 1800948 (2019).
40. Liangsupree, T., Multia, E. & Riekkola, M.-L. Modern isolation and separation techniques for extracellular vesicles. *J. Chromatogr. A* **1636**, 461773 (2021).
41. Lötval, J. et al. Minimal experimental requirements for definition of extracellular vesicles and their functions: a position statement from the International Society for Extracellular Vesicles. *J. Extracell. Vesicles* **3**, 26913 (2014).
42. Kashkanova, A. D. et al. Label-free discrimination of extracellular vesicles from large lipoproteins. *J. Extracell. Vesicles* **12**, e12348 (2023).
43. Geekiyanage et al. Extracellular microRNAs in human circulation are associated with miRISC complexes that are accessible to anti-AGO2 antibody and can bind target mimic oligonucleotides. *Proc. Natl Acad. Sci. USA* **117**, 24213–24223 (2020).
44. Rai, A. et al. Exosomes derived from human primary and metastatic colorectal cancer cells contribute to functional heterogeneity of activated fibroblasts by reprogramming their proteome. *Proteomics* **19**, e1800148 (2019).
45. Rai, A. et al. Secreted midbody remnants are a class of extracellular vesicles molecularly distinct from exosomes and microparticles. *Commun. Biol.* **4**, 400 (2021).
46. Rai, A., Greening, D. W., Xu, R., Suwakulsiri, W. & Simpson, R. J. Exosomes derived from the human primary colorectal cancer cell line SW480 Orchestrate Fibroblast-led Cancer Invasion. *Proteomics* **20**, e2000016 (2020).
47. Xu, R., Greening, D. W., Rai, A., Ji, H. & Simpson, R. J. Highly-purified exosomes and shed microvesicles isolated from the human colon cancer cell line LIM1863 by sequential centrifugal ultrafiltration are biochemically and functionally distinct. *Methods* **87**, 11–25 (2015).
48. Midekessa, G. et al. Zeta potential of extracellular vesicles: toward understanding the attributes that determine colloidal stability. *ACS Omega* **5**, 16701–16710 (2020).
49. Farrah, T. et al. A high-confidence human plasma proteome reference set with estimated concentrations in PeptideAtlas. *Mol. Cell Proteom.* **10**, M110 006353 (2011).
50. Kowal, J. et al. Proteomic comparison defines novel markers to characterize heterogeneous populations of extracellular vesicle subtypes. *Proc. Natl Acad. Sci. USA* **113**, E968–E977 (2016).
51. Minciacci, V. R. et al. Large oncosomes contain distinct protein cargo and represent a separate functional class of tumor-derived extracellular vesicles. *Oncotarget* **6**, 11327–11341 (2015).
52. Anderson, N. L. & Anderson, N. G. The human plasma proteome: history, character, and diagnostic prospects. *Mol. Cell Proteom.* **1**, 845–867 (2002).
53. Moon, M. J. et al. Differential effects of physiological agonists on the proteome of platelet-derived extracellular vesicles. *Proteomics* **24**, e2300391 (2024).
54. Auber, M. & Svenningsen, P. An estimate of extracellular vesicle secretion rates of human blood cells. *J. Extracell. Biol.* **1**, e46 (2022).
55. Alberro, A., Iparraguirre, L., Fernandes, A. & Otaegui, D. Extracellular vesicles in blood: sources, effects, and applications. *Int. J. Mol. Sci.* **22**, 8163 (2021).
56. Uhlen, M. et al. Proteomics. Tissue-based map of the human proteome. *Science* **347**, 1260419 (2015).
57. Oh, H. S. et al. Organ aging signatures in the plasma proteome track health and disease. *Nature* **624**, 164–172 (2023).

58. Eid, S., Turk, S., Volkamer, A., Rippmann, F. & Fulle, S. KinMap: a web-based tool for interactive navigation through human kinome data. *BMC Bioinf.* **18**, 16 (2017).
59. Bausch-Fluck, D. et al. The in silico human surfaceome. *Proc. Natl Acad. Sci. USA* **115**, E10988–E10997 (2018).
60. Cook, K. B., Kazan, H., Zuberi, K., Morris, Q. & Hughes, T. R. RBPDB: a database of RNA-binding specificities. *Nucleic Acids Res.* **39**, D301–D308 (2011).
61. Lambert, S. A. et al. The human transcription factors. *Cell* **172**, 650–665 (2018).
62. Robinson, H. et al. Caveolin-1-driven membrane remodelling regulates hnRNP-mediated exosomal microRNA sorting in cancer. *Clin. Transl. Med.* **11**, e381 (2021).
63. Xia, H. F. et al. PCBP2-dependent secretion of miRNAs via extracellular vesicles contributes to the EGFR-driven angiogenesis. *Theranostics* **15**, 1255–1271 (2025).
64. Matyasi, B. et al. Extracellular vesicle-mediated metastasis suppressors NME1 and NME2 modify lipid metabolism in fibroblasts. *Cancers* **14**, 3913 (2022).
65. Ye, C. et al. Src family kinases engage differential pathways for encapsulation into extracellular vesicles. *J. Extracell. Biol.* **2**, e96 (2023).
66. Li, W. et al. TGFβ1 in fibroblasts-derived exosomes promotes epithelial–mesenchymal transition of ovarian cancer cells. *Oncotarget* **8**, 96035–96047 (2017).
67. Hoshino, A. et al. Tumour exosome integrins determine organotropic metastasis. *Nature* **527**, 329–335 (2015).
68. Rai, A., Fang, H., Claridge, B., Simpson, R. J. & Greening, D. W. Proteomic dissection of large extracellular vesicle surfaceome unravels interactive surface platform. *J. Extracell. Vesicles* **10**, e12164 (2021).
69. Nunez Lopez, Y. O. et al. Proteomics and phosphoproteomics of circulating extracellular vesicles provide new insights into diabetes pathobiology. *Int. J. Mol. Sci.* **23**, 5779 (2022).
70. Karimi, N., Dalirfardouei, R., Dias, T., Lotvall, J. & Lasser, C. Tetraspanins distinguish separate extracellular vesicle subpopulations in human serum and plasma—contributions of platelet extracellular vesicles in plasma samples. *J. Extracell. Vesicles* **11**, e12213 (2022).
71. Kapustin, A. N. et al. Calcium regulates key components of vascular smooth muscle cell-derived matrix vesicles to enhance mineralization. *Circ. Res.* **109**, e1–e12 (2011).
72. Danjo, A. et al. Cystatin C stimulates the differentiation of mouse osteoblastic cells and bone formation. *Biochem. Biophys. Res. Commun.* **360**, 199–204 (2007).
73. Meng, L. B. et al. TPM2 as a potential predictive biomarker for atherosclerosis. *Aging* **11**, 6960–6982 (2019).
74. England, J. et al. Tropomyosin 1: Multiple roles in the developing heart and in the formation of congenital heart defects. *J. Mol. Cell. Cardiol.* **106**, 1–13 (2017).
75. Kiermayer, C. et al. Heart-specific knockout of the mitochondrial thioredoxin reductase (Txnrd2) induces metabolic and contractile dysfunction in the aging myocardium. *J. Am. Heart Assoc.* **4**, e002153 (2015).
76. Harayama, T. & Riezman, H. Understanding the diversity of membrane lipid composition. *Nat. Rev. Mol. Cell Biol.* **19**, 281–296 (2018).
77. Skotland, T., Sagini, K., Sandvig, K. & Llorente, A. An emerging focus on lipids in extracellular vesicles. *Adv. Drug Deliv. Rev.* **159**, 308–321 (2020).
78. Trajkovic, K. et al. Ceramide triggers budding of exosome vesicles into multivesicular endosomes. *Science* **319**, 1244–1247 (2008).
79. Stocker, R., Bowry, V. W. & Frei, B. Ubiquinol-10 protects human low density lipoprotein more efficiently against lipid peroxidation than does alpha-tocopherol. *Proc. Natl Acad. Sci. USA* **88**, 1646–1650 (1991).
80. Jha, P. et al. Genetic regulation of plasma lipid species and their association with metabolic phenotypes. *Cell Syst.* **6**, 709–721 e6 (2018).
81. Stafford, J. H. & Thorpe, P. E. Increased exposure of phosphatidylethanolamine on the surface of tumor vascular endothelium. *Neoplasia* **13**, 299–308 (2011).
82. Leite, N. B. et al. PE and PS lipids synergistically enhance membrane poration by a peptide with anticancer properties. *Biophys. J.* **109**, 936–947 (2015).
83. Dinkins, M. B., Dasgupta, S., Wang, G., Zhu, G. & Bieberich, E. Exosome reduction in vivo is associated with lower amyloid plaque load in the 5XFAD mouse model of Alzheimer's disease. *Neurobiol. Aging* **35**, 1792–1800 (2014).
84. Sezgin, E., Levental, I., Mayor, S. & Eggeling, C. The mystery of membrane organization: composition, regulation and roles of lipid rafts. *Nat. Rev. Mol. Cell Biol.* **18**, 361–374 (2017).
85. Nakai, W. et al. A novel affinity-based method for the isolation of highly purified extracellular vesicles. *Sci. Rep.* **6**, 33935 (2016).
86. Yim, K. H. W., Krzyzaniak, O., Al Hrou, A., Peacock, B. & Chahwan, R. Assessing extracellular vesicles in human biofluids using flow-based analyzers. *Adv. Health. Mater.* **12**, e2301706 (2023).
87. Tosetti, F. et al. Specific ADAM10 inhibitors localize in exosome-like vesicles released by Hodgkin lymphoma and stromal cells and prevent sheddase activity carried to bystander cells. *Oncoimmunology* **7**, e1421889 (2018).
88. Mu, W., Rana, S. & Zoller, M. Host matrix modulation by tumor exosomes promotes motility and invasiveness. *Neoplasia* **15**, 875–887 (2013).
89. Harada, Y. et al. Generation of the heterogeneity of extracellular vesicles by membrane organization and sorting machineries. *Biochim. Biophys. Acta, Gen. Subj.* **1863**, 681–691 (2019).
90. Dooley, K. et al. A versatile platform for generating engineered extracellular vesicles with defined therapeutic properties. *Mol. Ther.* **29**, 1729–1743 (2021).
91. Lespagnol, A. et al. Exosome secretion, including the DNA damage-induced p53-dependent secretory pathway, is severely compromised in TSAP6/Steap3-null mice. *Cell Death Differ.* **15**, 1723–1733 (2008).
92. Cvjetkovic, A. et al. Detailed analysis of protein topology of extracellular vesicles-evidence of unconventional membrane protein orientation. *Sci. Rep.* **6**, 36338 (2016).
93. Babuke, T. & Tikkanen, R. Dissecting the molecular function of reggie/flotillin proteins. *Eur. J. Cell Biol.* **86**, 525–532 (2007).
94. Skryabin, G. O., Komelkov, A. V., Savelyeva, E. E. & Tchekina, E. M. Lipid rafts in exosome biogenesis. *Biochem. (Mosc.)* **85**, 177–191 (2020).
95. Kajimoto, T., Okada, T., Miya, S., Zhang, L. & Nakamura, S. Ongoing activation of sphingosine 1-phosphate receptors mediates maturation of exosomal multivesicular endosomes. *Nat. Commun.* **4**, 2712 (2013).
96. Baietti, M. F. et al. Syndecan-syntenin-ALIX regulates the biogenesis of exosomes. *Nat. Cell Biol.* **14**, 677–685 (2012).
97. Zhang, X. L., Topley, N., Ito, T. & Phillips, A. Interleukin-6 regulation of transforming growth factor (TGF)-beta receptor compartmentalization and turnover enhances TGF-beta1 signaling. *J. Biol. Chem.* **280**, 12239–12245 (2005).
98. Lietha, D. & Izard, T. Roles of membrane domains in integrin-mediated cell adhesion. *Int. J. Mol. Sci.* **21**, 5531 (2020).
99. Arcaro, A. et al. Critical role for lipid raft-associated Src kinases in activation of PI3K–Akt signalling. *Cell Signal* **19**, 1081–1092 (2007).
100. Mukhopadhyay, N. K. et al. Heterogeneous nuclear ribonucleoprotein K is a novel regulator of androgen receptor translation. *Cancer Res.* **69**, 2210–2218 (2009).
101. Inder, K. L. et al. Expression of PTRF in PC-3 cells modulates cholesterol dynamics and the actin cytoskeleton impacting secretion pathways. *Mol. Cell Proteom.* **11**, M111 012245 (2012).

102. Inder, K. L. et al. Cavin-1/PTRF alters prostate cancer cell-derived extracellular vesicle content and internalization to attenuate extracellular vesicle-mediated osteoclastogenesis and osteoblast proliferation. *J. Extracell. Vesicles* **3**, 23784 (2014).
103. Ji, H. et al. Deep sequencing of RNA from three different extracellular vesicle (EV) subtypes released from the human LIM1863 colon cancer cell line uncovers distinct miRNA-enrichment signatures. *PLoS ONE* **9**, e110314 (2014).
104. Tauro, B. J. et al. Two distinct populations of exosomes are released from LIM1863 colon carcinoma cell-derived organoids. *Mol. Cell Proteom.* **12**, 587–598 (2013).
105. Tkach, M., Kowal, J. & Thery, C. Why the need and how to approach the functional diversity of extracellular vesicles. *Philos. Trans. R. Soc. Lond. B* **373**, 20160479 (2018).
106. Al-Nedawi, K. et al. Intercellular transfer of the oncogenic receptor EGFRvIII by microvesicles derived from tumour cells. *Nat. Cell Biol.* **10**, 619–624 (2008).
107. Wiklander, O. P. et al. Extracellular vesicle in vivo biodistribution is determined by cell source, route of administration and targeting. *J. Extracell. Vesicles* **4**, 26316 (2015).
108. Larsen, J. H., Jensen, I. S. & Svenningsen, P. Benchmarking transcriptome deconvolution methods for estimating tissue- and cell-type-specific extracellular vesicle abundances. *J. Extracell. Vesicles* **13**, e12511 (2024).
109. Li, Y. et al. EV-origin: Enumerating the tissue-cellular origin of circulating extracellular vesicles using exLR profile. *Comput. Struct. Biotechnol. J.* **18**, 2851–2859 (2020).
110. Brahmer, A. et al. Platelets, endothelial cells and leukocytes contribute to the exercise-triggered release of extracellular vesicles into the circulation. *J. Extracell. Vesicles* **8**, 1615820 (2019).
111. Wiklander, O. P. B. et al. Systematic methodological evaluation of a multiplex bead-based flow cytometry assay for detection of extracellular vesicle surface signatures. *Front. Immunol.* **9**, 1326 (2018).
112. Wild-Bode, C., Fellerer, K., Kugler, J., Haass, C. & Capell, A. A basolateral sorting signal directs ADAM10 to adherens junctions and is required for its function in cell migration. *J. Biol. Chem.* **281**, 23824–23829 (2006).
113. Xu, N. et al. ARPC4 promotes bladder cancer cell invasion and is associated with lymph node metastasis. *J. Cell. Biochem.* **121**, 231–243 (2020).
114. Dufour, S. et al. Nanoscale imaging of CD47 informs how plasma membrane modifications shape apoptotic cell recognition. *Commun. Biol.* **6**, 207 (2023).
115. Naik, U. P., Naik, M. U., Eckfeld, K., Martin-DeLeon, P. & Spychala, J. Characterization and chromosomal localization of JAM-1, a platelet receptor for a stimulatory monoclonal antibody. *J. Cell Sci.* **114**, 539–547 (2001).
116. Wrobel, L., Hoffmann, J. L., Li, X. & Rubinsztein, D. C. p37 regulates VCP/p97 shuttling and functions in the nucleus and cytosol. *Sci. Adv.* **10**, ead16082 (2024).
117. Cote, M. et al. Munc18-2 deficiency causes familial hemophagocytic lymphohistiocytosis type 5 and impairs cytotoxic granule exocytosis in patient NK cells. *J. Clin. Invest.* **119**, 3765–3773 (2009).
118. Maxwell, K. N., Zhou, Y. & Hancock, J. F. Rac1 nanoscale organization on the plasma membrane is driven by lipid binding specificity encoded in the membrane anchor. *Mol. Cell Biol.* **38**, e00186–18 (2018).
119. Welch, M. D., DePace, A. H., Verma, S., Iwamatsu, A. & Mitchison, T. J. The human Arp2/3 complex is composed of evolutionarily conserved subunits and is localized to cellular regions of dynamic actin filament assembly. *J. Cell Biol.* **138**, 375–384 (1997).
120. Lee, S. et al. Transport through recycling endosomes requires EHD1 recruitment by a phosphatidylserine translocase. *EMBO J.* **34**, 669–688 (2015).
121. Glebov, O. O., Bright, N. A. & Nichols, B. J. Flotillin-1 defines a clathrin-independent endocytic pathway in mammalian cells. *Nat. Cell Biol.* **8**, 46–54 (2006).
122. Michetti, M. et al. Autolysis of human erythrocyte calpain produces two active enzyme forms with different cell localization. *FEBS Lett.* **392**, 11–15 (1996).
123. Tiger, C. F., Fougereuse, F., Grundstrom, G., Velling, T. & Gullberg, D. $\alpha 1\beta 1$ integrin is a receptor for interstitial collagens involved in cell migration and collagen reorganization on mesenchymal nonmuscle cells. *Dev. Biol.* **237**, 116–129 (2001).
124. Chae, T. H., Kim, S., Marz, K. E., Hanson, P. I. & Walsh, C. A. The hyh mutation uncovers roles for alpha Snap in apical protein localization and control of neural cell fate. *Nat. Genet.* **36**, 264–270 (2004).
125. Hanafusa, K. & Hayashi, N. The Flot2 component of the lipid raft changes localization during neural differentiation of P19C6 cells. *BMC Mol. Cell Biol.* **20**, 38 (2019).
126. Mukhopadhyay, A., Funato, K. & Stahl, P. D. Rab7 regulates transport from early to late endocytic compartments in *Xenopus* oocytes. *J. Biol. Chem.* **272**, 13055–13059 (1997).
127. Zhou, K. et al. Actin-related protein2/3 complex regulates tight junctions and terminal differentiation to promote epidermal barrier formation. *Proc. Natl Acad. Sci. USA* **110**, E3820–E3829 (2013).
128. Zhang, R. et al. Actin polymerization inhibition by targeting ARPC2 affects intestinal stem cell homeostasis. *Burns Trauma* **11**, tkad038 (2023).
129. Xia, Z. et al. GNA13 regulates BCL2 expression and the sensitivity of GCB-DLBCL cells to BCL2 inhibitors in a palmitoylation-dependent manner. *Cell Death Dis.* **12**, 54 (2021).
130. Nakata, Y., Tomkowicz, B., Gewirtz, A. M. & Ptasznik, A. Integrin inhibition through Lyn-dependent cross talk from CXCR4 chemokine receptors in normal human CD34⁺ marrow cells. *Blood* **107**, 4234–4239 (2006).
131. Silva, J. M. et al. Cyfip1 is a putative invasion suppressor in epithelial cancers. *Cell* **137**, 1047–1061 (2009).
132. Ruppelt, A. et al. Inhibition of T cell activation by cyclic adenosine 5'-monophosphate requires lipid raft targeting of protein kinase A type I by the A-kinase anchoring protein ezrin. *J. Immunol.* **179**, 5159–5168 (2007).
133. Chieragatti, E., Chicka, M. C., Chapman, E. R. & Baldini, G. SNAP-23 functions in docking/fusion of granules at low Ca²⁺. *Mol. Biol. Cell* **15**, 1918–1930 (2004).
134. Hurley, J. H. & Hanson, P. I. Membrane budding and scission by the ESCRT machinery: it's all in the neck. *Nat. Rev. Mol. Cell Biol.* **11**, 556–566 (2010).
135. Sjolín, C., Movitz, C., Lundqvist, H. & Dahlgren, C. Translocation of annexin XI to neutrophil subcellular organelles. *Biochim. Biophys. Acta* **1326**, 149–156 (1997).
136. Knecht, S., Eberl, H. C. & Bantscheff, M. Interval-based secretomics unravels acute-phase response in hepatocyte model systems. *Mol. Cell Proteom.* **21**, 100241 (2022).
137. Wei, W. et al. Cell type-selective secretome profiling in vivo. *Nat. Chem. Biol.* **17**, 326–334 (2021).
138. Naughton, M. A. et al. Organ-specific contribution to circulating C7 levels by the bone marrow and liver in humans. *Eur. J. Immunol.* **26**, 2108–2112 (1996).
139. Haslund, D. et al. Dominant-negative SERPING1 variants cause intracellular retention of C1 inhibitor in hereditary angioedema. *J. Clin. Invest.* **129**, 388–405 (2019).
140. Mittenbuhler, M. J. et al. Isolation of extracellular fluids reveals novel secreted bioactive proteins from muscle and fat tissues. *Cell Metab.* **35**, 535–549 (2023).

141. VerHague, M. A., Cheng, D., Weinberg, R. B. & Shelness, G. S. Apolipoprotein A-IV expression in mouse liver enhances triglyceride secretion and reduces hepatic lipid content by promoting very low density lipoprotein particle expansion. *Arterioscler. Thromb. Vasc. Biol.* **33**, 2501–2508 (2013).
142. Baringer, S. L., Palsa, K., Spiegelman, V. S., Simpson, I. A. & Connor, J. R. Apo- and holo-transferrin differentially interact with hephaestin and ferroportin in a novel mechanism of cellular iron release regulation. *J. Biomed. Sci.* **30**, 36 (2023).
143. Ruf, M. et al. SERPINC1 c.1247dupC: a novel SERPINC1 gene mutation associated with familial thrombosis results in a secretion defect and quantitative antithrombin deficiency. *Thromb. J.* **22**, 19 (2024).
144. Dreismann, A. K. et al. Functional expression of complement factor I following AAV-mediated gene delivery in the retina of mice and human cells. *Gene Ther.* **28**, 265–276 (2021).
145. Barallobre-Barreiro, J. et al. Extracellular matrix remodelling in response to venous hypertension: proteomics of human varicose veins. *Cardiovasc. Res.* **110**, 419–430 (2016).
146. Mihara, E. et al. Active and water-soluble form of lipidated Wnt protein is maintained by a serum glycoprotein afamin/alpha-albumin. *eLife* **5**, e11621 (2016).
147. Pieragostino, D. et al. Shotgun proteomics reveals specific modulated protein patterns in tears of patients with primary open angle glaucoma naive to therapy. *Mol. Biosyst.* **9**, 1108–1116 (2013).
148. Anderson, N. L. et al. The human plasma proteome: a nonredundant list developed by combination of four separate sources. *Mol. Cell Proteom.* **3**, 311–326 (2004).
149. Palmer, D. J. et al. Human colostrum: identification of minor proteins in the aqueous phase by proteomics. *Proteomics* **6**, 2208–2216 (2006).
150. Watanabe, J. et al. Hemoglobin and its scavenger protein haptoglobin associate with apoA-1-containing particles and influence the inflammatory properties and function of high density lipoprotein. *J. Biol. Chem.* **284**, 18292–18301 (2009).
151. Kiernan, U. A., Tubbs, K. A., Nedelkov, D., Niederkofler, E. E. & Nelson, R. W. Comparative phenotypic analyses of human plasma and urinary retinol binding protein using mass spectrometric immunoassay. *Biochem. Biophys. Res. Commun.* **297**, 401–405 (2002).
152. Didangelos, A. et al. Proteomics characterization of extracellular space components in the human aorta. *Mol. Cell Proteom.* **9**, 2048–2062 (2010).
153. Jones, D., Morgan, C. & Cockcroft, S. Phospholipase D and membrane traffic. Potential roles in regulated exocytosis, membrane delivery and vesicle budding. *Biochim. Biophys. Acta* **1439**, 229–244 (1999).
154. Foster, D. A. Phosphatidic acid signaling to mTOR: signals for the survival of human cancer cells. *Biochim. Biophys. Acta* **1791**, 949–955 (2009).
155. van der Veen, J. N., Lingrell, S. & Vance, D. E. The membrane lipid phosphatidylcholine is an unexpected source of triacylglycerol in the liver. *J. Biol. Chem.* **287**, 23418–23426 (2012).
156. Exton, J. H. Phosphatidylcholine breakdown and signal transduction. *Biochim. Biophys. Acta* **1212**, 26–42 (1994).
157. Dawaliby, R. et al. Phosphatidylethanolamine is a key regulator of membrane fluidity in eukaryotic cells. *J. Biol. Chem.* **291**, 3658–3667 (2016).
158. Bogdanov, M. & Dowhan, W. Phospholipid-assisted protein folding: phosphatidylethanolamine is required at a late step of the conformational maturation of the polytopic membrane protein lactose permease. *EMBO J.* **17**, 5255–5264 (1998).
159. Nagata, S., Suzuki, J., Segawa, K. & Fujii, T. Exposure of phosphatidylserine on the cell surface. *Cell Death Differ.* **23**, 952–961 (2016).
160. Kay, J. G., Koivusalo, M., Ma, X., Wohland, T. & Grinstein, S. Phosphatidylserine dynamics in cellular membranes. *Mol. Biol. Cell* **23**, 2198–2212 (2012).
161. Muralidharan, S. et al. A reference map of sphingolipids in murine tissues. *Cell Rep.* **35**, 109250 (2021).
162. Yamaguchi, T., Hirakawa, R. & Ochiai, H. Correlation between sphingomyelin and the membrane stability of mammalian erythrocytes. *Comp. Biochem. Physiol. B* **265**, 110833 (2023).
163. Gulshan, K., Brubaker, G., Wang, S., Hazen, S. L. & Smith, J. D. Sphingomyelin depletion impairs anionic phospholipid inward translocation and induces cholesterol efflux. *J. Biol. Chem.* **288**, 37166–37179 (2013).
164. Baillet, L., Mullur, R. S., Esser, V. & McGarry, J. D. Elucidation of the mechanism by which (+)-acylcarnitines inhibit mitochondrial fatty acid transport. *J. Biol. Chem.* **275**, 36766–36768 (2000).
165. Dumesnil, C. et al. Cholesterol esters form supercooled lipid droplets whose nucleation is facilitated by triacylglycerols. *Nat. Commun.* **14**, 915 (2023).
166. Liu, J., Fike, K. R., Dapper, C. & Klemba, M. Metabolism of host lysophosphatidylcholine in *Plasmodium falciparum*-infected erythrocytes. *Proc. Natl Acad. Sci. USA* **121**, e2320262121 (2024).
167. Furse, S. & de Kroon, A. I. Phosphatidylcholine's functions beyond that of a membrane brick. *Mol. Membr. Biol.* **32**, 117–119 (2015).
168. Saito, R. F., Andrade, L. N. S., Bustos, S. O. & Chammas, R. Phosphatidylcholine-derived lipid mediators: the crosstalk between cancer cells and immune cells. *Front. Immunol.* **13**, 768606 (2022).
169. Boumann, H. A. et al. Depletion of phosphatidylcholine in yeast induces shortening and increased saturation of the lipid acyl chains: evidence for regulation of intrinsic membrane curvature in a eukaryote. *Mol. Biol. Cell* **17**, 1006–1017 (2006).
170. Wallner, S. et al. Phosphatidylcholine and phosphatidylethanolamine plasmalogens in lipid loaded human macrophages. *PLoS ONE* **13**, e0205706 (2018).
171. Kimura, T., Kimura, A. K. & Epand, R. M. Systematic crosstalk in plasmalogen and diacyl lipid biosynthesis for their differential yet concerted molecular functions in the cell. *Prog. Lipid Res.* **91**, 101234 (2023).
172. Martin, T. F. Phosphoinositides as spatial regulators of membrane traffic. *Curr. Opin. Neurobiol.* **7**, 331–338 (1997).
173. van Dierendonck, X. et al. Triglyceride breakdown from lipid droplets regulates the inflammatory response in macrophages. *Proc. Natl Acad. Sci. USA* **119**, e2114739119 (2022).
174. Deshwal, S. et al. Mitochondria regulate intracellular coenzyme Q transport and ferroptotic resistance via STARD7. *Nat. Cell Biol.* **25**, 246–257 (2023).

Publisher's note Springer Nature remains neutral with regard to jurisdictional claims in published maps and institutional affiliations.

Open Access This article is licensed under a Creative Commons Attribution 4.0 International License, which permits use, sharing, adaptation, distribution and reproduction in any medium or format, as long as you give appropriate credit to the original author(s) and the source, provide a link to the Creative Commons licence, and indicate if changes were made. The images or other third party material in this article are included in the article's Creative Commons licence, unless indicated otherwise in a credit line to the material. If material is not included in the article's Creative Commons licence and your intended use is not permitted by statutory regulation or exceeds the permitted use, you will need to obtain permission directly from the copyright holder. To view a copy of this licence, visit <http://creativecommons.org/licenses/by/4.0/>.

© The Author(s) 2025

Methods

Generation of cell conditioned media

SW480 (CCL-288, ATCC), SW620 (CCL-227, ATCC) and LIM1863 cells¹⁷⁵ (Ludwig Institute for Cancer Research, Melbourne) cells were cultured in RPMI-1640 (Life Technologies). MDA MB 231 (HTB-26, ATCC) was cultured in Dulbecco's modified Eagle medium (Life Technologies). Primary human cell sources included the human neonatal foreskin fibroblast cell line (neoHFF) (kindly provided by P. Kaur, Australia) and adult human dermal fibroblasts (Gibco/Thermo Fisher Scientific, #C0135C). These cells were cultured in complete culture media supplemented with 5% (v/v) foetal bovine serum (FBS, Life Technologies) and 1% (v/v) penicillin–streptomycin (Life Technologies). Human atrial cardiac fibroblasts (Lonza, #CC-2903) and human ventricular cardiac fibroblasts (Lonza, #CC-2904) were cultured in FGM-3 Cardiac Fibroblast Growth Medium-3 BulletKit (Lonza, #CC-3131 and #CC-4525). Human umbilical vein endothelial cells (HUVEC, Lonza, #CC-2519; HUVEC sourced as gift (K. Peter, BMDI, Australia), HUVEC-RFP, Angio-Proteomie #cAP-0001) were cultured in EGM-2 Endothelial Cell Growth Medium-2 BulletKit (Lonza #CC-3156 and #CC-4176 supplements) prepared as detailed by the supplier. All cells were cultured at 37 °C with 10% CO₂ as described^{45,68}. Cells were passaged with trypsin–EDTA (Gibco). Cells were cultured in CELLline AD-1000 Bioreactor classic flasks (Integra Biosciences) for conditioned media generation as described⁶⁸.

Plasma preparation

Human blood plasma samples were obtained from Australian Red Cross Lifeblood, the EDCAD study or the AusDiab trial. For Red Cross, ethical permits were obtained from the Australian Red Cross Blood Service Human Research Ethics Committee, and La Trobe University Human Ethics Committee (HEC19485). Blood samples were collected via aseptic venipuncture into commercial EDTA-containing sampling containers at room temperature and centrifuged at 4,200g for 10 min. The top plasma supernatant was carefully collected and further centrifuged at 5,000g (15 min) at room temperature. The supernatant was immediately isolated and stored as 1-ml aliquots at –80 °C until further use. For EDCAD samples, ethics permit was approved through the Human Research Ethics Committee at Baker Heart and Diabetes Institute and by the Alfred Hospital Ethics Committee (EDCAD-PMS, #492/20). Blood was collected via venipuncture into a sterile EDTA tube and centrifuged at 2,700g at room temperature for 13 min. A small volume (1.6 ml) of the supernatant (plasma) was transferred into a clean sterile tube, and butylated hydroxytoluene solution (BHT) was added to a final concentration of 100 µM. The plasma/BHT sample was mixed and equally transferred into 3×0.75 ml Fluid X cryotubes. Plasma/BHT samples were snap frozen on dry ice before being transferred and stored at –80 °C until use). For AusDiab trial samples, the ethics permit was approved through the Human Research Ethics Committee at Baker Heart and Diabetes Institute and by the Alfred Hospital Ethics Committee (#39/11). Blood was collected into commercial fluoride/oxalate tubes and centrifuged at 2,500 rpm for 10 min at room temperature. Plasma was isolated and snap frozen on dry ice before being transferred and stored at –80 °C until use. Clinical parameters for EDCAD plasma samples are provided in Supplementary Table 41.

For all plasma collections, only ~80% of top plasma supernatant was collected to avoid disturbing the buffy coat. Samples with potential haemolysis, cellular contamination and high fat/lipid content were not used for this study.

Ultracentrifugation of plasma or conditioned media

To generate crude 100 K plasma pellet, plasma samples were thawed on ice and subjected to ultracentrifugation at 100,000g for 1 h or 18 h at 4 °C (TLA-55 rotor; Optima MAX-MP Tabletop Ultracentrifuge, Beckman Coulter). Pellets were washed once in 1.0 ml phosphate-buffered saline (PBS), resuspended in 100 µl PBS and stored at –80 °C until further use.

Human fibroblasts and endothelial cells (80% confluent in T75 culture flasks) were cultured in Dulbecco's modified Eagle medium supplemented with 0.5% v/v insulin transferrin selenium (Invitrogen) and 1% penicillin–streptomycin to generate conditioned media. To isolate EVs, we subjected conditioned media to differential centrifugation (500g for 5 min and 2,000g for 10 min at 4 °C), followed by concentration using Amicon Ultra Centrifugal Filter, 100 kDa molecular weight cut-off (low-speed centrifugation at 2,000g at 4 °C). The filter was washed five times with 1 ml ice-cold PBS. The concentrated retentate was retrieved and further centrifuged at 10,000g (30 min at 4 °C) to pellet crude large EVs (10 K EVs), while the resultant supernatant underwent ultracentrifugation at 100,000g (1 h at 4 °C) to pellet crude small EVs (100 K EVs). The isolated EVs were washed in PBS (1 ml, 10,000g for large EVs and 100,000g for small EVs) before resuspension in 50 µl PBS and stored at –80 °C until further use (subsequent proteomic and lipidomic analyses).

Direct density-gradient separation

Plasma (500 µl) was directly overlaid on top of discontinuous gradient of OptiPrep (40% (3 ml), 20% (3 ml), 10% (3 ml) and 5% (2.5 ml) (diluent: PBS solution)) and ultracentrifuged at 100,000g for 18 h (4 °C, 41 Ti rotor; Optima XPN Ultracentrifuge). Twelve 1-ml fractions were carefully collected from top to bottom, diluted in PBS (2 ml) and ultracentrifuged at 100,000g (1 h, 4 °C, TLA-55 rotor; Optima MAX-MP Tabletop Ultracentrifuge). Fraction densities were determined as previously described⁴⁵. Pellets were suspended in 100 µl PBS and stored at –80 °C until further use. For bottom-up DGS, 500 µl of plasma was carefully loaded at the bottom of a preformed discontinuous DGS (OptiPrep (40% (3 ml), 20% (3 ml), 10% (3 ml) and 5% (2.5 ml) (diluent: PBS solution)) using a long syringe to avoid disturbing the gradient. Ultracentrifugation was performed at 100,000g for 18 h (4 °C), as in the top-loaded DGS method. After centrifugation, 12 equal fractions (1 ml each) were collected, diluted with 2 ml PBS and subjected to another round of ultracentrifugation at 100,000g for 1 h (4 °C). The resulting pellets were resuspended in 50 µl PBS and analysed by western blotting.

For the isolation of cell culture-derived EVs, the conditioned medium was centrifuged at 500g (5 min, 4 °C), 2,000g (10 min, 4 °C) and 10,000g (30 min, 4 °C, SW28 rotor; Optima XPN Ultracentrifuge, Beckman Coulter) to pellet large EVs⁶⁸. The supernatant (1 ml) was subjected to direct DGS for EV isolation as described for plasma above. EV pellets were reconstituted in 100 µl PBS and stored at –80 °C until further use.

Immunoblotting

Samples were subjected to protein quantification (microBCA Protein Assay Kit (23235, Thermo Fisher Scientific)), and western blotting (iBlot 2 Dry Blotting System, Thermo Fisher Scientific) was performed as described^{45,68}. Rabbit antibodies raised against albumin (ab207327, Abcam) and AGO2 (ab186733, Abcam) were used. Mouse antibodies CD63 (556019, BD Pharmingen), CD81 (555675, BD Pharmingen), APOB100 (3715-3-250, Mabtech) and APOA1 (3710-3-1000, Mabtech) were used (1:1,000). Secondary antibodies used were IRDye 800 goat anti-mouse IgG or IRDye 700 goat anti-rabbit IgG (1:15000, LI-COR Biosciences).

Biophysical characterization of EVs

Cryo-electron microscopy (Tecnai G2 F30) on samples (1 µg) was performed as described⁴⁷. In brief, Plasma 100 K, D-DGS fractions 1–3 (pooled) and pEVs (DGS fractions 6–8, pooled) (~1 µg) were loaded onto glow-discharged C-flat holey carbon grids (ProSciTech Pty) that, after blotting away excess liquid, were plunge-frozen in liquid ethane and subsequently mounted in a Gatan cryoholder (Gatan) in liquid nitrogen. Images were then acquired at 300 kV using a Tecnai G2 F30 (FEI) in low-dose mode. EV samples (~1 µg; 1:1,000 dilution) were

prepared in PBS (#14190-144, Thermo Fisher Scientific)¹⁷⁶, and particle size distribution and zeta potential (surface charge) were determined by nanoparticle tracking analysis (ZetaView, Particle Metrix, PMX-120; 405-nm laser diode) according to manufacturers' instructions.

Surface biotin labelling of EVs and proteomic sample preparation

EV surface proteins (from SW620 cells, $n = 3$ biological replicates) were captured using the Pierce Cell Surface Biotinylation and Isolation Kit (A44390, Thermo Fisher Scientific) and digested with trypsin (Promega, V5111), and the resulting peptides were analysed using the Q-Exactive HF-X, as previously described⁶⁸.

Label-free proteomics sample preparation

Label-free proteomics sample preparation (~ 2 – $10 \mu\text{g}$ in 20 – $50 \mu\text{l}$) was performed as described based on the single-pot solid-phase-enhanced sample preparation (SP3) workflow⁶⁸. Protein sets were digested with trypsin and Lys-C (1:50 and 1:100 enzyme-to-protein ratio, respectively), and peptide digests were frozen at -80°C and lyophilized by vacuum-based speedVac (Savant SPD121P, Thermo Fisher Scientific), reconstituted in 0.07% trifluoroacetic acid and quantified by fluorometric peptide assay (23290, Thermo Fisher Scientific).

TMT-based proteomics sample preparation

TMT-based labelling was performed as described¹⁷⁷, using 10-plex TMT according to the manufacturer's instructions with modifications (Thermo Fisher Scientific, 90406, lot UG287488/278919). The 10-plex experiment included nine different chemical tags for EV peptide labelling, with the tenth tag used as a reference channel generated from a pooled peptide digest of all samples. A list of the sample labelling strategy is available in MassIVE proteomeXchange ([MSV000094307](https://proteomecentral.org/proteomeXchange/MSV000094307)). Peptide samples ($15.5 \mu\text{g}$) were labelled with TMT10plex Isobaric Label (90406, Thermo Fisher Scientific) at 4:1 label-to-peptide ratio for 2 h at room temperature and quenched with 0.5% (v/v) hydroxylamine for 30 min at room temperature. Labelled peptide samples were acidified with 4% (v/v) formic acid (FA) and pooled into a new microtube. Pooled samples were desalted using Sep-Pak tC18 96-well $\mu\text{Elution}$ plates (186002318, Waters), and the eluates were lyophilized using a SpeedVac. Peptides were fractionated into 20 fractions (with increasing concentration of acetonitrile from 2% to 50%) using high-pH reversed-phase chromatography with in-house SPE StageTips (SDB-RPS, Empore). Peptide eluates were lyophilized, reconstituted in 0.07% trifluoroacetic acid (TFA) and quantified using a colorimetric peptide assay. Peptide fractions with low yields were pooled.

Nano liquid chromatography (LC)–MS/MS

Peptides (label-free and TMT-labelled) were analysed in randomized sequence batches on a Dionex UltiMate NCS-3500RS nanoUHPLC coupled to a Q-Exactive HF-X hybrid quadrupole-Orbitrap mass spectrometer equipped with nanospray ion source operating in positive mode as described^{68,178}.

For label-free proteomics, peptides were loaded (Acclaim Pep-Map100 C18 $3\text{-}\mu\text{m}$ beads with 100 \AA pore size, Thermo Fisher Scientific) and separated ($1.9\text{-}\mu\text{m}$ particle size C18, $0.075 \times 250 \text{ mm}$, Nikkyo Technos) with a gradient of 2 – 28% acetonitrile containing 0.1% FA over 49 or 95 min at 300 nl min^{-1} at 55°C (butterfly portfolio heater, Phoenix S&T).

For data-dependent acquisition (DDA), MS1 scan was acquired from 350 to $1,650 m/z$ ($60,000$ resolution, 3×10^6 automatic gain control (AGC), 128 ms injection time) followed by MS/MS DDA (top 25) with collision-induced dissociation and detection in the ion trap ($30,000$ resolution, 1×10^5 AGC target, 27 ms injection time, 28% normalized collision energy, $1.3 m/z$ quadrupole isolation width). Unassigned and precursor ions with charge states 1 and 6–8 were rejected, and peptide match was disabled. Selected sequenced ions were dynamically excluded for 30 s . Data were acquired using Xcalibur software v4.0.

For data independent acquisition (DIA)¹⁷⁹, full-scan MS was performed in the m/z range of 350 – $1,100 m/z$ with a $60,000$ resolution, using an AGC of 3×10^6 , maximum injection time of 50 ms and 1 microscan . MS2 was set to $15,000$ resolution, with an AGC target of 1×10^6 and the first fixed mass set to $120 m/z$. The default charge state was set to 2 and recorded in centroid mode. Total scan windows (38 windows; 49-min gradient, 63 windows, 95-min gradient) with a staggered isolation window from 350 to $1,100 m/z$ were applied with 28% normalized collision energy.

TMT-labelled peptides were separated ($1.9 \mu\text{m}$ particle size C18, $0.075 \times 250 \text{ mm}$, Nikkyo Technos) with a gradient of 4 – 28% acetonitrile containing 0.1% FA over 110 min at 300 nl min^{-1} at 55°C (butterfly portfolio heater, Phoenix S&T). The MS1 scan was acquired from 300 to $1,650 m/z$ ($60,000$ resolution, 3×10^6 AGC, 128 ms injection time) followed by MS/MS DDA of the top 15 ions with higher-energy collisional dissociation (HCD) ($30,000$ resolution, 1×10^5 automatic gain control (AGC), 60 ms injection time, 33 normalized collision energy (NCE), $0.8 m/z$ isolation width). Unassigned precursor ions and those with charge states 1 and 6–8 were rejected, and peptide matching was disabled. Selected sequenced ions were dynamically excluded for 30 s .

MS-based proteomics data (including sample/label annotation) are deposited to the ProteomeXchange Consortium via the MassIVE partner repository and available via MassIVE with identifier [MSV000094307](https://proteomecentral.org/proteomeXchange/MSV000094307).

Proteomic data processing

For DDA and TMT proteomics, peptide identification and quantification were performed using MaxQuant (v1.6.6.0–v1.6.14) with its built-in search engine Andromeda as described⁶⁸ against *Homo sapiens* (UP000005640) including the contaminants database. For label-free quantification-based analyses (DDA), cysteine carbamidomethylation was selected as a fixed modification and N-terminal acetylation and methionine oxidations as variable modifications. Data were processed using trypsin/P as the proteolytic enzymes with up to two missed cleavage sites allowed. Further processing was performed using the 'match between runs' feature and the label-free quantification algorithm. Peptides were identified with an initial precursor mass deviation of up to 7 ppm and a fragment mass deviation of 20 ppm with a minimum length of 7 amino acids. FDR was 0.01 for both the protein and peptide by searching against a reverse database. For TMT-based analyses, reporter ion MS2 (TMT10plex) settings were used. For biotin surface proteome analysis, an additional thioacyl (DSP, $\text{C}_3\text{H}_4\text{OS}$) was used⁴⁷.

For DIA proteomics, data processing was performed using DIA-NN¹⁸⁰ (v1.8). Spectral libraries were predicted using the neural network deep learning algorithm used in DIA-NN with trypsin/P, allowing up to one missed cleavage. The precursor change range was set to 1–4, and the m/z precursor range was set to 300 – $1,800$ for peptides consisting of 7–30 amino acids. N-terminal methionine excision and cysteine carbamidomethylation were enabled as fixed modifications, with the maximum number of variable modifications set to zero. The mass spectra were analysed using default settings with a FDR of 1% for precursor identifications and match between runs enabled for replicates. Contaminants and reverse identifications were removed from the resulting output files.

Lipid extraction

Lipid extraction was performed using a modified single-phase butanol/methanol extraction method as described¹⁸¹. Samples (2 – $5 \mu\text{g}$ protein from lyophilized sample in $10 \mu\text{l}$ of water) were mixed with $100 \mu\text{l}$ of 1:1 butanol:methanol containing internal standards; the samples were vortexed, sonicated on a sonicator bath (1 h) and centrifuged ($13,000g$, 10 min). The supernatants were transferred into glass vials and stored at -80°C . Before MS analysis, samples were thawed for 1 h at room temperature, vortexed, sonicated in a sonication bath for 15 min and then left to equilibrate at 20°C for 2 h before analysis.

LC-MS (discovery)

Analysis of lipid extracts was performed (in randomized sequence batches) on an Agilent 6495C QQQ mass spectrometer with an Agilent 1290 series high-performance LC (HPLC) system, including a ZORBAX eclipse plus C18 (2.1×100 mm $1.8 \mu\text{m}$, Agilent) rapid resolution high-throughput column. MS settings and transitions for each lipid class are provided (Supplementary Table 40), adapted from previous methodology¹⁸². Conditions included: gas temperature 150°C , gas flow rate 17 l min^{-1} , nebulizer gas pressure 20 psi, sheath gas temperature 200°C , capillary voltage 3,500 V and sheath gas flow 10 l min^{-1} . Isolation widths for Q1 and Q3 were set to 'unit' resolution (0.7 amu). HPLC conditions included solvent A (50:30:20 water:acetonitrile:isopropanol) and solvent B (1:9:90 water:acetonitrile:isopropanol), with a gradient of 15–100% solvent B over 16 min (total runtime: 20 min), at a flow rate of 0.4 ml min^{-1} and a column compartment temperature of 45°C . Solvent A was buffered with 10 mM ammonium formate with medronic acid, while solvent B was buffered with 10 mM ammonium formate.

LC-MS (validation) for AusDiab and fibroblasts/endothelial cell EVs

Analysis of lipid extracts was performed on an Agilent 6495C QQQ mass spectrometer with an Agilent 1290 series HPLC system similar to the discovery analysis. Mass spectrometer conditions were as follows: gas temperature 200°C , gas flow rate 17 l min^{-1} , nebulizer gas pressure 20 psi, sheath gas temperature 280°C , capillary voltage 3,500 V and sheath gas flow 10 l min^{-1} . Isolation widths for Q1 and Q3 were set to 'unit' resolution (0.7 amu). Solvent composition was as per discovery run, with a modified gradient of 15–100% B, over 11 min (total runtime 16 min), at 0.4 ml min^{-1} and column compartment at 45°C . Further characterization was performed on PC, PC(O) and PC(P) isobaric and isomeric species to highlight the separation resolution of the rapid resolution high throughput (RRHT) column (Supplementary Fig. 21).

Lipid data integration and statistical analysis

Raw lipidomic MS data were analysed using MassHunter Quant 10.0 (Agilent Technologies). The peak area of lipid species was normalized to their respective internal standards to generate relative concentration data per sample. For lipids that appear to have isomeric separation on the chromatography, they are designated with the (a) and (b) annotations to highlight different elution orders. Lipid class totals were generated by summing the individual species within each class. MS-based lipidomic RAW data and sample/label annotations have been deposited in the ProteomeXchange Consortium via the MassIVE partner repository and are available under the identifier [MSV000094307](https://proteomecentral.proteomexchange.org/protein/PXD00094307).

Structural characterization of lipid isomers and isobars

As PS 36:1 represented a strong signature for EVs, we determined the structure of this PS species in isolated EVs, we reran pooled samples under negative ionization mode under the same gradient conditions, screening for product ions corresponding to the serine head group ($788.5 \text{ m/z} \rightarrow 701.5 \text{ m/z}$) and the fatty acyl tails. The final composition was annotated to be PS 18:0_18:1, with signals observed with 283.3 and 281.3 product ions (Supplementary Fig. 20). The method used for these samples monitors CEs in positive ionization mode as ammonium adducts, tracking the COH ion along with an additional water loss ($\text{CE } 18:0 \text{ [M} + \text{NH}_4] + 670.6/369.3$). A matching internal standard ($\text{CE } 18:0\text{-d}_6$) was used to quantify this lipid species. Retention time, mass and fragmentation patterns were used to confirm its annotation.

Nanoflow analysis of pEVs

pEVs ($\sim 5 \mu\text{g}$) were subjected to fixation and permeabilization using eBioscience Foxp3/Transcription Factor Staining Buffer Set (Invitrogen, 00-5523-00). In brief, pEVs (in $50 \mu\text{l}$ PBS) were incubated with $500 \mu\text{l}$ fixation and permeabilization buffer on ice for 30 min. Samples were ultracentrifuged at $100,000\text{g}$ (1 h at 4°C), and pellets were

resuspended in $100 \mu\text{l}$ wash buffer. Samples were stained with $5 \mu\text{l}$ APC Annexin V reagent (BioLegend) and $2 \mu\text{g}$ of either anti-ADAM 10 antibody (Sigma-Aldrich, AB19026) or rabbit IgG Isotype Control (Invitrogen, 10500C). Samples were incubated at room temperature (gentle end-over mixing) for 1 h. Samples were topped with $900 \mu\text{l}$ wash buffer and washed twice (ultracentrifuged at $100,000\text{g}$ (1 h at 4°C)) to remove remaining antibodies and potential antibody aggregates. The pellets were resuspended in $100 \mu\text{l}$ wash buffer containing $0.5 \mu\text{l}$ of goat anti-rabbit Alexa Fluor 568 Dye secondary antibody (Thermo Fisher Scientific) incubated for 30 min at room temperature (gentle end-over mixing) in the dark. Samples were topped with $900 \mu\text{l}$ wash buffer and washed twice (ultracentrifuged at $100,000\text{g}$ (1 h at 4°C)). Pellets were resuspended in $100 \mu\text{l}$ of PBS (0.5% bovine serum albumin) using a $0.22\text{-}\mu\text{m}$ filter. Samples were immediately analysed using Cytex Aurora flow cytometer and SpectroFlo software, as previously described⁸⁶. In brief, controls included isotype control antibodies to assess non-specific binding, along with unstained EV suspensions and buffer-only controls. For purity assessment, SDS was added to labelled EVs at a final concentration of 0.5%, followed by vigorous vortexing for $\sim 30 \text{ s}$ before acquisition. High purity is indicated by a marked reduction in vesicle concentration and fluorescence following treatment. The instrument set-up was consistent across all experiments and followed recommendations from the manufacturer. Before the acquisition, the flow cell was washed with Contrad to minimize machine-associated noise. Instrument gating calibration was performed using 90-nm (#64009-15) 125-nm (#64011-15), 150-nm (#64012-15), 200-nm (#64013-15) and equal mix (90–200 nm) beads (Nanobead NIST Traceable Particle Size Standards). The threshold for side scatter was set to 430, and the gain of side scatter was set to 10. The YG3-A channel was used to detect the Alexa Fluor 568 signal, and the R1-A channel was used to detect the APC signal. For all samples, 10,000 events were recorded at the lowest flow rate to minimize the swarming effect. Statistical analysis of flow cytometry values was performed using GraphPad (v 9.1.0) using multiple paired *t*-tests.

Isolation of EVs using affinity to TIM4

To capture PS-positive EVs from plasma, human TIM4-Fc protein (FUJIFILM Wako Pure Chemical Corporation) was biotinylated with EZ-Link Maleimide-PEG11-Biotin (Thermo Fisher Scientific) and conjugated to Dynabeads MyOne Streptavidin C1 magnetic beads (65001, Thermo Fisher Scientific) as described¹⁸³. In brief, plasma ($200 \mu\text{l}$), diluted with $300 \mu\text{l}$ of PBS, was supplemented with heparin sodium (4U, Thermo Fisher Scientific) and CaCl_2 (final concentration of 2 mM) and incubated with TIM4 affinity beads for 16 hr at 4°C with gentle rotation. Beads were collected and washed $5\times$ with 1 ml Tween-TBS (0.05% Tween-20, 2 ml CaCl_2). EVs were eluted in $50 \mu\text{l}$ PBS containing 1 mM EDTA and subjected to DIA-based proteomic analyses as described.

Data processing and statistical analysis

Software tools used for this study are freely available as open-source R packages (<https://www.r-project.org>). No newly generated software or custom code were used in this current study, and hence, the codes have not been deposited in a public repository but are available from the corresponding author(s) upon request.

For key analyses, proteome and lipidome datasets were analysed using the R package Differential Enrichment analysis of Proteomics data (DEP)¹⁸⁴. Proteins identified in at least 70% of one biological group were selected for downstream analysis. Using DEP, the data were background-corrected and normalized by variance stabilizing transformation (vsN), which also performs \log_2 transformation. Missing values were then imputed: missing at random data were imputed using the 'knn' method, while missing not at random data were imputed using the 'MinProb' method. Protein-wise linear models combined with empirical Bayes statistics were used for the differential enrichment analysis, whereby the raw *P* values were adjusted to correct for multiple testing

using Benjamini–Hochberg method. Differentially abundant proteins or lipids were clustered by *k*-means clustering using the DEP package. The PCA plot, Pearson correlation matrix, volcano plots, log₂-centred bar plots and overlap bar plots were also generated using DEP. Heatmaps were generated using ComplexHeatmap package¹⁸⁵. Box plots and scatter plots were generated using RStudio package ggplot2. Cytoscape¹⁸⁶ was used to generate the Ontology map¹⁸⁷ (plugin v3.7.1). Bioconductor package clusterProfiler 4.0 (ref. 188) was used to perform GO and KEGG pathway enrichment analyses, as well as KEGG gene set enrichment analysis, with default parameters to identify significantly enriched gene sets. The pathway-based data integration and visualization was constructed using R package pathview¹⁸⁹. For identification of lipid-associated terms enriched in lipidomes, the LION web-based ontology enrichment tool¹⁹⁰ was used.

For conserved protein identification analysis, proteins were classified as detected or not detected across samples (protein abundance was not considered). In surface biotin labelling of EVs, proteins detected in at least six out of nine experiments were considered as pEV surface proteins (protein abundance was not considered). For annotating surface proteins into different categories, SURFY⁵⁹-based categorical annotation of cell surface proteins were used. To identify pEV lipid features, we performed *K*-means clustering of differentially abundant lipids between pEVs versus NonEVs and in vitro EVs versus cells using DEP package.

We used the caretEnsemble R package to assess the ability of these protein features (182 pEV protein features and 42 NonEV protein features, using the naive Bayes algorithm), surface protein features (comprising 151 surface proteins associating with pEV surface and 32 surface proteins associating with NonEVs, using the naive Bayes algorithm) or lipid features (114 pEV lipid features and 52 NonEV lipid features, using the neural network algorithm ('nnet')) to distinguish between distinguish between pEV and NonEV particles. The pEV and NonEV proteome/lipidome datasets were evenly partitioned based on sample type into a training set (70% of the samples) and a validation set (remaining 30% of samples). For protein features based machine learning, proteomes of pEVs (*n* = 16) and pDGS.LD (NonEV particles, *n* = 16) from as 16 plasma samples of the EDCAD cohort served as an independent test set. For lipid features-based machine learning, lipidomes of DGS plasma fractions served as an independent test set. A bootstrapping resampling method was used with 25 resampling iterations to train the models. The performance of the models was evaluated using class probabilities and the two-class summary function. The preprocessing steps of centring and scaling were applied to the predictors before training the models. A confusion matrix comparing predicted classes with actual classes, based on the machine learning algorithm used, was generated to visualize the model's predictive performance. For identification of ADAM10 protein or PS(36:1) and CE(18:0) lipids as biomarker candidates, RFE provided by the caret R package for feature selection using default options was used.

To address the question of source attribution in a data-driven manner, we manually curated tissue- and cell-type-specific protein signatures from three independent sources: (1) the Human Protein Atlas (HPA), which provides tissue- and organ-specific proteins based on immunohistochemistry (Extended Data Fig. 2a,b); (2) the HPA nTPM dataset, an RNA-derived protein expression database across tissues and cells (Extended Data Fig. 2c); and (3) organ-specific protein signatures detected in human plasma, identified via aptamer-based detection⁵⁷ (Extended Data Fig. 2d). To systematically assess the presence of bioactive molecules in pEVs, we manually curated and integrated multiple independent datasets that catalogue biologically significant protein classes. Specifically, we leveraged established resources for human transcription factors⁶¹ (Human TFs Database), RNA-binding proteins⁶⁰ (RBPDB Database), kinases⁵⁸ (KinHub Database) and cell-surface receptors, transporters and signalling proteins⁵⁹. In addition, we incorporated GO terms related to cytokine activity (GO:0005125), chemokine

activity (GO:0008009), growth factor activity (GO:0008083) and signal transduction (GO:0007165) to ensure comprehensive coverage of bioactive EV-associated molecules.

As a resource, the Shiny web application (<https://evmap.shinyapps.io/evmap/>) powered by R and hosted on shinyapps.io, was developed using the R packages shiny, gplots, and ComplexHeatmap. It offers feature selection and visualization tools for EV protein and lipid feature conservation in circulating EVs.

Statistics and reproducibility

All experiments were performed with at least three independent biological replicates unless otherwise specified. Each replicate was derived from separate cell culture preparations or human plasma samples to ensure biological variability as detailed in the corresponding figure legends. Conserved and differential expression (protein and lipid) analyses were not performed blind due to the conditions of the experiments. No data were excluded from the analyses. The raw *P* values were adjusted to correct for multiple testing using the Benjamini–Hochberg method and are reported in the corresponding figure legends and supplementary tables. The statistical tests were chosen on the basis of the data distribution and experimental design. The quantitative data are presented as the mean or median ± standard error of the mean as indicated in the text or figure legends. Statistical analyses were conducted using R or GraphPad Prism. Proteome and lipidome datasets were vsn-normalized, but normality and variance were not formally tested. No statistical methods were used to predetermine sample sizes; the sample sizes were determined on the basis of previously published studies and pilot experiments. All key findings were independently validated in at least three separate experiments, and reproducibility was confirmed across different experimental set-ups, plasma source or cell lines when applicable.

Reporting summary

Further information on research design is available in the Nature Portfolio Reporting Summary linked to this article.

Data availability

The data supporting the findings presented are available within this Resource or its Supplementary Information or source data files. All of the data supporting the findings of this study are further available from the corresponding author upon reasonable request. The raw MS files (proteome and lipidome), sample/label annotation (Source Data 3) and the search/identification files obtained using MaxQuant/DIA-NN have been deposited to the ProteomeXchange Consortium via the MassIVE partner repository and available via MassIVE with identifier [MSV000094307](https://proteomecentral.proteomexchange.org/protein?id=MSV000094307). Source data are provided with this paper.

References

- Whitehead, R. H., Jones, J. K., Gabriel, A. & Lukies, R. E. A new colon carcinoma cell line (LIM1863) that grows as organoids with spontaneous differentiation into crypt-like structures in vitro. *Cancer Res.* **47**, 2683–2689 (1987).
- Lozano, J. et al. Scalable generation of nanovesicles from human-induced pluripotent stem cells for cardiac repair. *Int. J. Mol. Sci.* **23**, 14334 (2022).
- Bond, S. T. et al. Mitochondrial damage in muscle specific PolG mutant mice activates the integrated stress response and disrupts the mitochondrial folate cycle. *Nat. Commun.* **16**, 2338 (2025).
- Fang, H. et al. Proteomics and machine learning-based approach to decipher subcellular proteome of mouse heart. *Mol. Cell Proteom.* **24**, 100952 (2025).
- Cross, J., Rai, A., Fang, H., Claridge, B. & Greening, D. W. Rapid and in-depth proteomic profiling of small extracellular vesicles for ultralow samples. *Proteomics* **24**, e2300211 (2023).

180. Demichev, V., Messner, C. B., Vernardis, S. I., Lilley, K. S. & Ralser, M. DIA-NN: neural networks and interference correction enable deep proteome coverage in high throughput. *Nat. Methods* **17**, 41–44 (2020).
181. Huynh, K. et al. Concordant peripheral lipidome signatures in two large clinical studies of Alzheimer's disease. *Nat. Commun.* **11**, 5698 (2020).
182. Huynh, K. et al. High-throughput plasma lipidomics: detailed mapping of the associations with cardiometabolic risk factors. *Cell Chem. Biol.* **26**, 71–84 e4 (2019).
183. Yoshida, T., Ishidome, T. & Hanayama, R. High purity isolation and sensitive quantification of extracellular vesicles using affinity to TIM4. *Curr. Protoc. Cell Biol.* **77**, 3 45 1–3 45 18 (2017).
184. Zhang, X. et al. Proteome-wide identification of ubiquitin interactions using UblA-MS. *Nat. Protoc.* **13**, 530–550 (2018).
185. Gu, Z., Eils, R. & Schlesner, M. Complex heatmaps reveal patterns and correlations in multidimensional genomic data. *Bioinformatics* **32**, 2847–2849 (2016).
186. Shannon, P. et al. Cytoscape: a software environment for integrated models of biomolecular interaction networks. *Genome Res.* **13**, 2498–2504 (2003).
187. Merico, D., Isserlin, R., Stueker, O., Emili, A. & Bader, G. D. Enrichment map: a network-based method for gene-set enrichment visualization and interpretation. *PLoS ONE* **5**, e13984 (2010).
188. Wu, T. et al. clusterProfiler 4.0: a universal enrichment tool for interpreting omics data. *Innovation* **2**, 100141 (2021).
189. Luo, W. & Brouwer, C. Pathview: an R/Bioconductor package for pathway-based data integration and visualization. *Bioinformatics* **29**, 1830–1831 (2013).
190. Molenaar, M. R. et al. LION/web: a web-based ontology enrichment tool for lipidomic data analysis. *Gigascience* **8**, giz061 (2019).
191. Liberzon, A. et al. The Molecular Signatures Database (MSigDB) hallmark gene set collection. *Cell Syst.* **1**, 417–425 (2015).

Acknowledgements

The D.W.G. laboratory is supported by research funds from the National Health and Medical Research Council (NHMRC, MRF2015523, APP1141946), National Heart Foundation (NHF, 105072), Helen Amelia Hains Fellowship (D.W.G.) and Department of Defense (PR230065). The Baker Heart and Diabetes Institute acknowledges support by

the Victorian State Government Operational Infrastructure funding. The funders had no role in the study design, data collection and analysis, decision to publish or preparation of the manuscript. We thank E. Hanssen and the Bio21 Molecular Science and Biotechnology Institute for assisting cryo-electron microscopy (University of Melbourne). K.H. is supported by an NHMRC Emerging Leadership Fellowship (GNT1197190). Q.H.P., H.F. and B.C. are supported through an Australian RFP Scholarship, in addition to the Bright Sparks Foundation. Schematic figures were created with [BioRender.com](https://www.biorender.com).

Author contributions

A.R. and D.W.G. conceptualized the idea. A.R. designed the experiments and wrote the manuscript. A.R., Q.H.P., H.F., B.C., J.C., T.D., C.D. and D.W.G. performed experiments. A.R. performed bioinformatics analysis. A.R., K.H. and D.W.G. analysed the results. C.D., J.E.S. and T.H.M. provided resources. A.R. developed the software/app. D.W.G. acquired funding. A.R., K.H., B.C., J.E.S., T.H.M., P.M. and D.W.G. reviewed the manuscript for submission.

Funding

Open access funding provided by La Trobe University

Competing interests

The authors declare no conflicts of interest.

Additional information

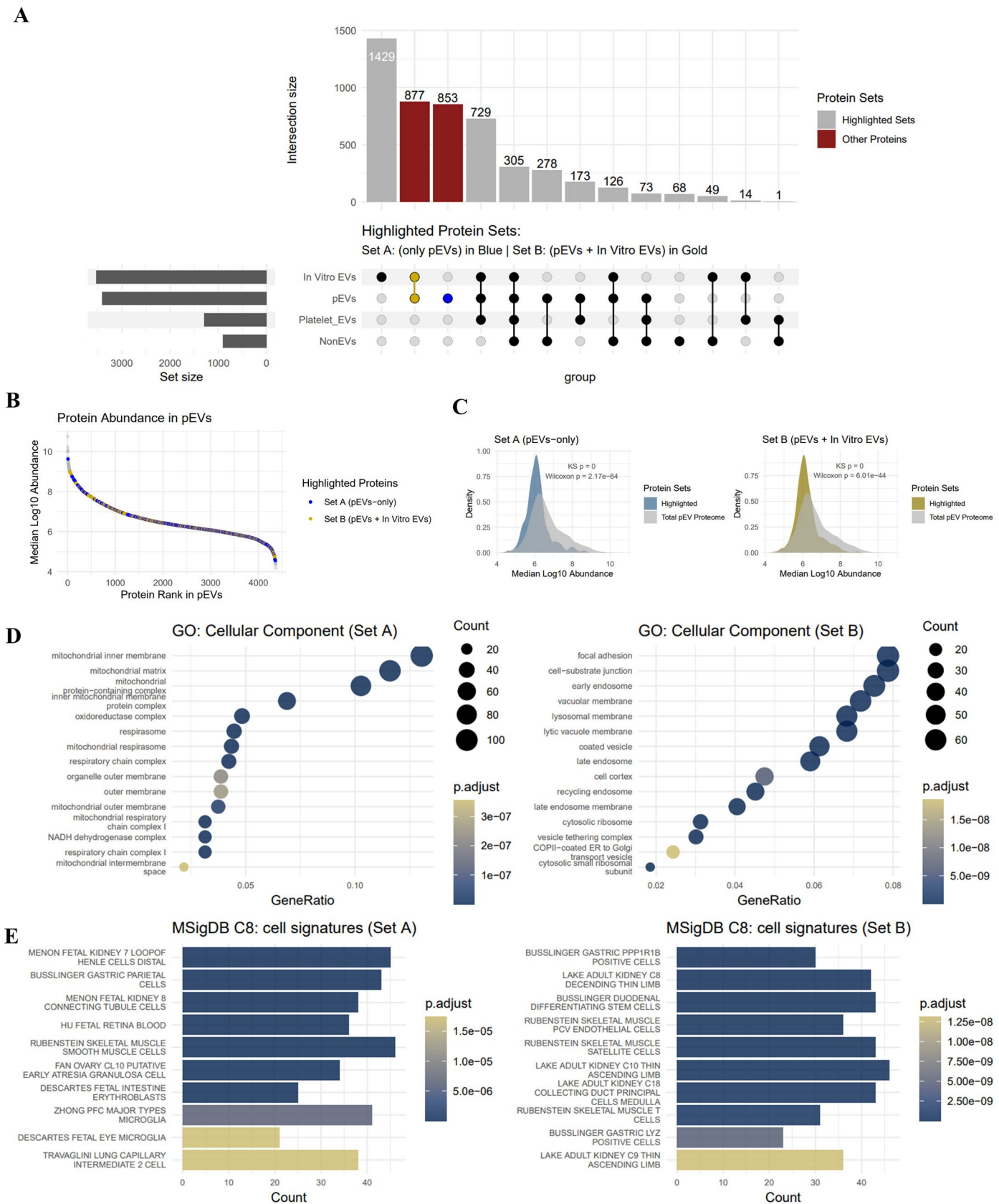
Extended data is available for this paper at <https://doi.org/10.1038/s41556-025-01795-7>.

Supplementary information The online version contains supplementary material available at <https://doi.org/10.1038/s41556-025-01795-7>.

Correspondence and requests for materials should be addressed to Alin Rai or David W. Greening.

Peer review information *Nature Cell Biology* thanks Fong-Fu Hsu and the other, anonymous, reviewer(s) for their contribution to the peer review of this work. Peer reviewer reports are available.

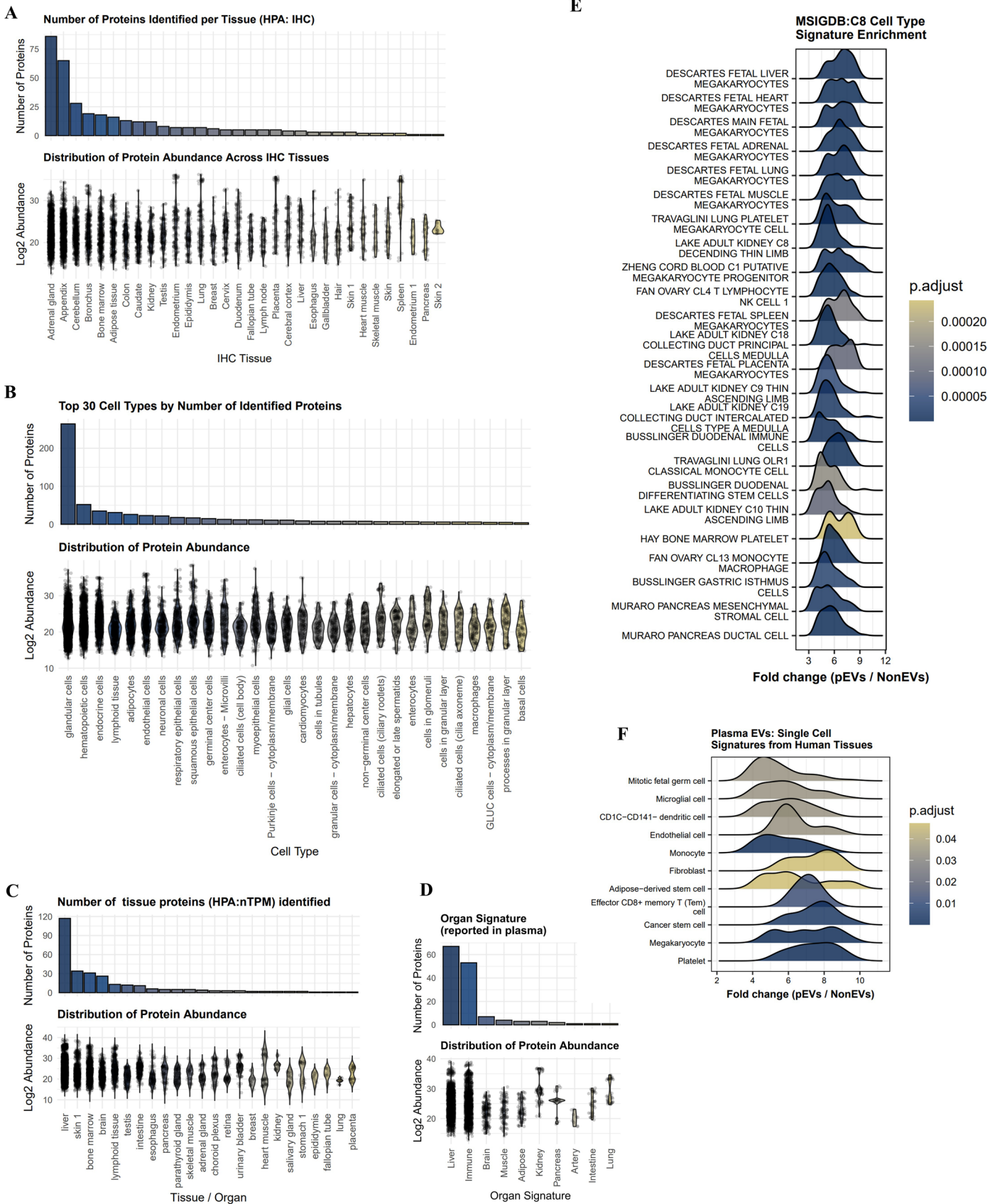
Reprints and permissions information is available at www.nature.com/reprints.



Extended Data Fig. 1 | Diverse cellular source attribution to pEV proteome.

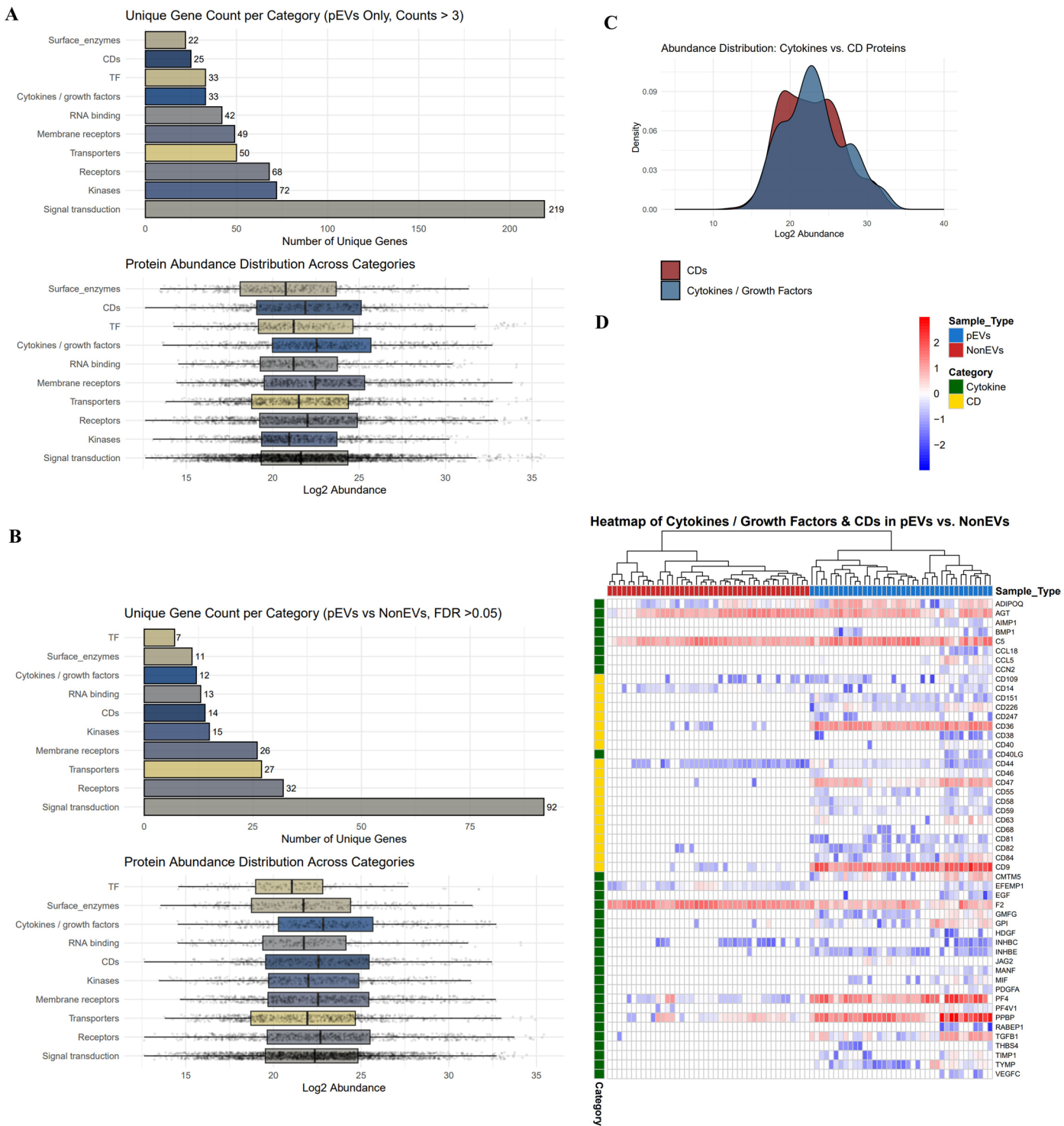
A. Distribution of activated platelet EV proteins in pEVs and in vitro EVs. Set A and Set B proteins represent proteins quantified exclusively in pEVs and in vitro EVs versus activated platelet EVs⁵³. **B.** Distribution of Set A and Set B proteins (abundance) in pEV proteome. **C.** Density plots of Set A and Set B

protein abundance vs pEV proteome abundance. **D.** Gene Ontology (Cellular Component) analysis of Set A and Set B proteins (Benjamini-Hochberg corrected $p.adjust < 0.05$). **E.** Gene Set Enrichment Analysis (using Molecular signature database⁹¹ for cell signatures (C8 category)) of Set A and Set B proteins (Benjamini-Hochberg corrected $p.adjust < 0.05$).



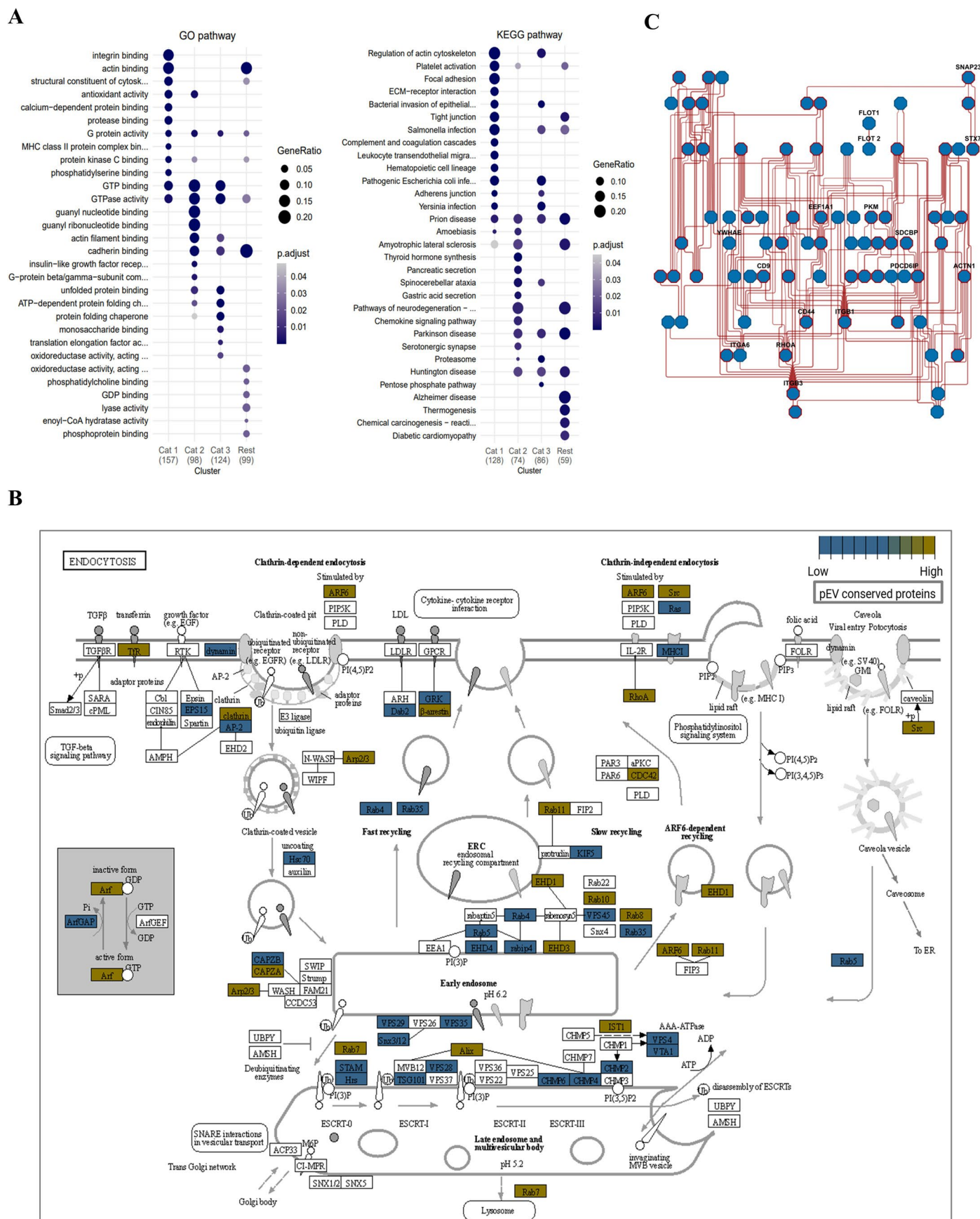
Extended Data Fig. 2 | Quantification of tissue / organ-associated proteins in pEVs. **A.** Number of tissue-associated proteins (based on Human Protein Atlas (HPA) immunohistochemistry data (IHC)⁵⁶) quantified in pEV proteome. Abundance distribution of proteins are presented in lower panel. **B.** Number of cell-type-associated proteins (based on HPA IHC) quantified in pEV proteome. Abundance distribution of proteins is presented in lower panel. **C.** Number of tissue-associated proteins (based on HPA normalized transcript per million (nTPM)) quantified in pEV proteome. Abundance distribution of proteins is presented in lower panel. **D.** Number of organ-associated proteins reported in

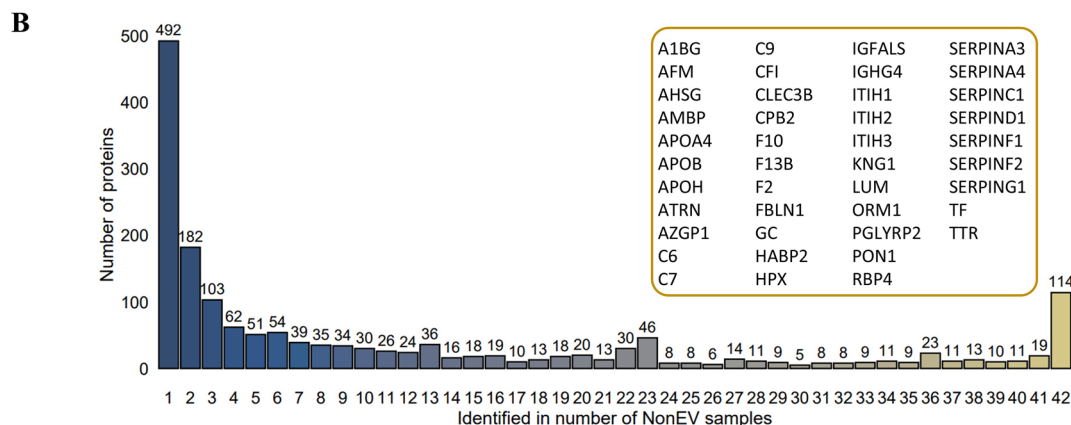
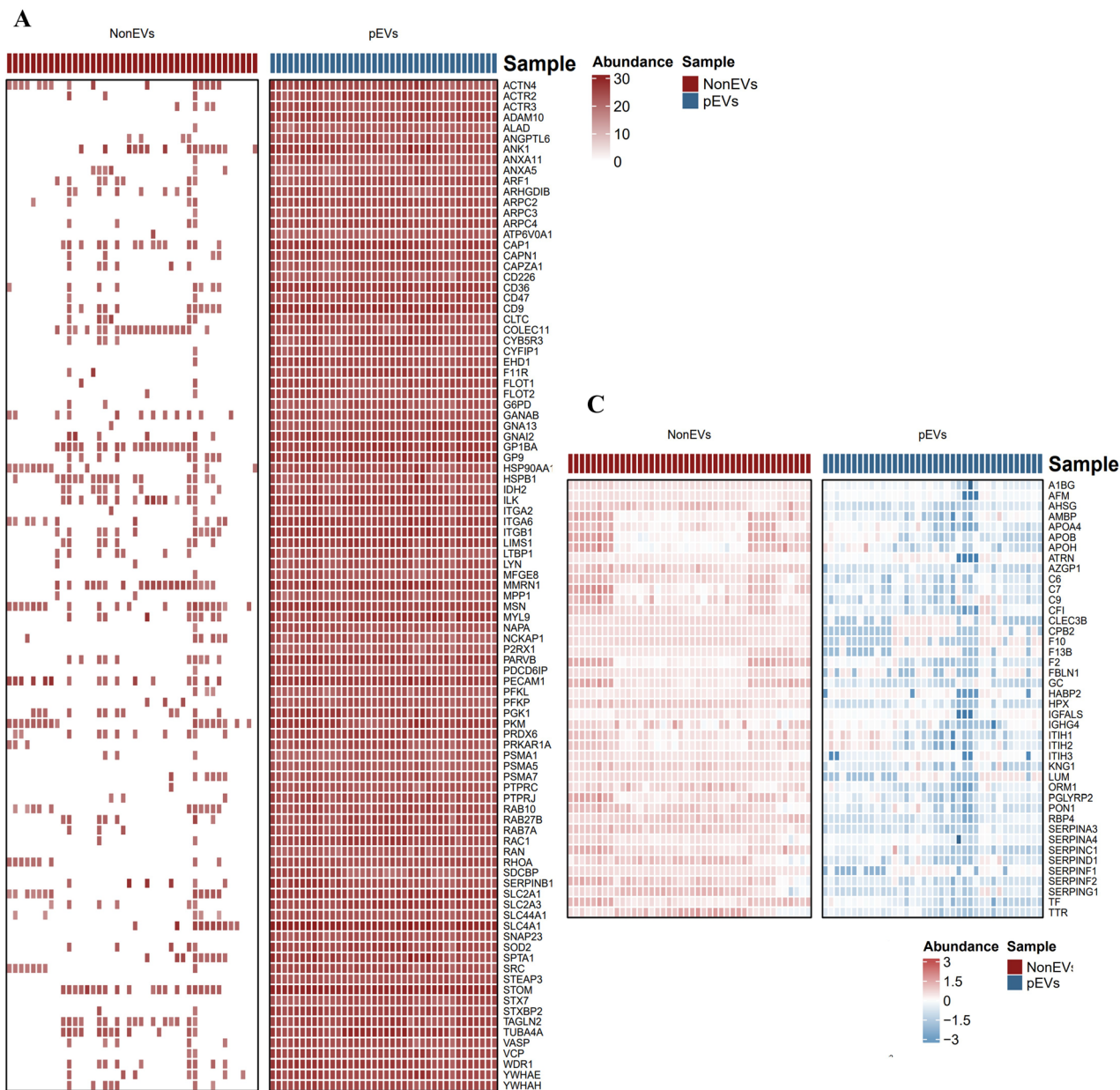
plasma using aptamers quantified in pEV proteome⁵⁷. Abundance distribution of these proteins is presented in lower panel. Violin plots in **A-D** show the distribution of log2 protein abundance (individual points are overlaid). **E.** Gene Set Enrichment Analysis (using Molecular signature database⁴⁹ for cell signatures (C8 category) of proteins enriched in pEV versus NonEV proteomes (Benjamini-Hochberg corrected $p.adjust < 0.05$). **F.** Enrichment of cell signatures based on single-cell sequencing studies of human tissue⁴⁹ in proteins enriched pEV versus NonEVs. (Benjamini-Hochberg corrected $p.adjust < 0.05$).



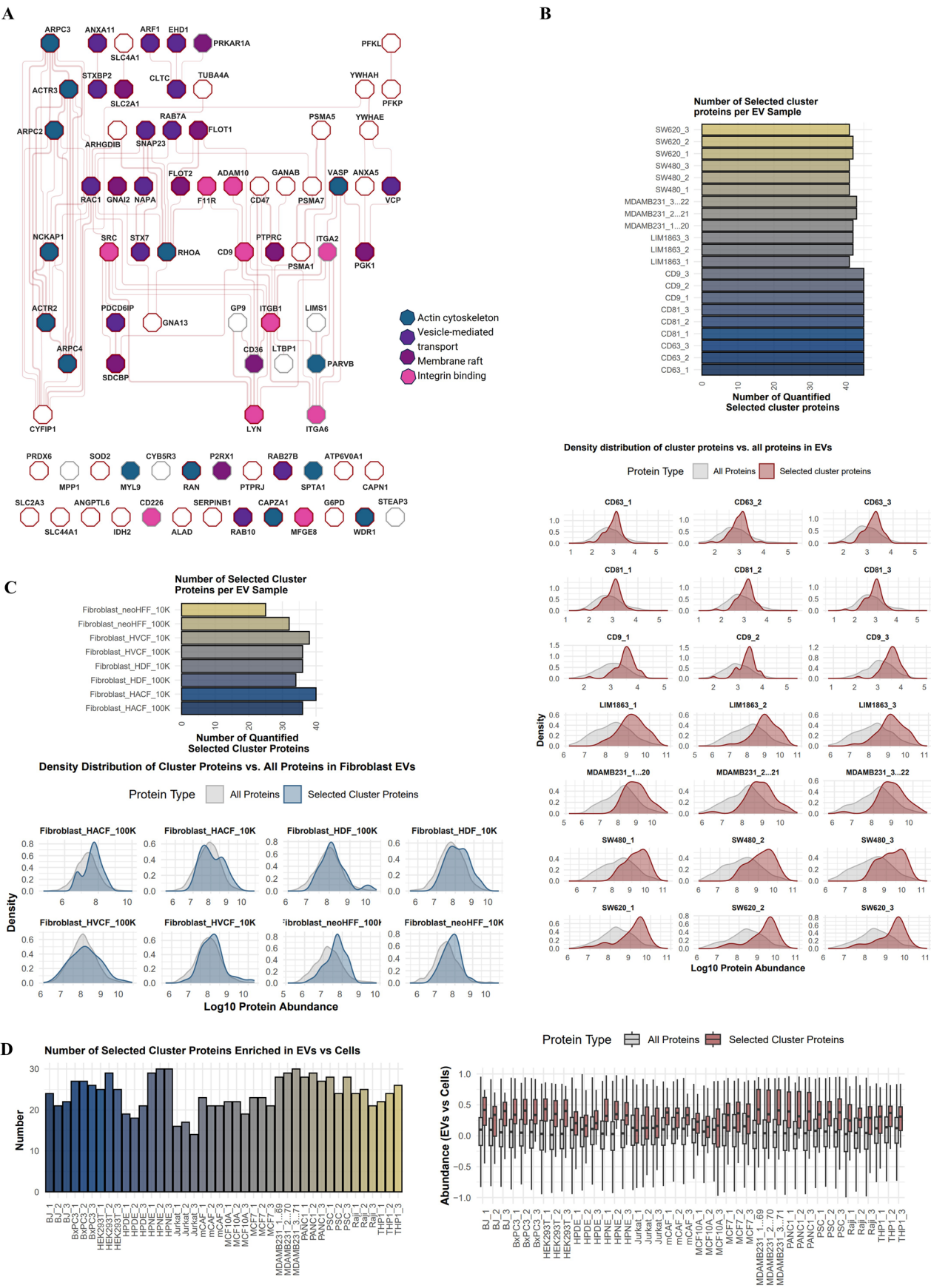
Extended Data Fig. 3 | Diversity of bioactive cargo in pEVs. A. Number of different cargo-type quantified in pEV proteomes (in at least 3 out of 38 pEV proteomes, independent plasma samples), with boxplot in lower panel representing protein abundance distribution. TF, transcription factors; CDs, Cluster of Differentiation. Gene Ontology terms related to cytokine activity (GO:0005125), chemokine activity (GO:0008009), growth factor activity (GO:0008083), and signal transduction (GO:0007165) to ensure comprehensive coverage of bioactive EV-associated molecules **B.** Number of different cargo-type quantified in pEV proteomes (but significantly enriched in pEVs vs NonEVs,

FDR < 0.05, n = 38 pEV proteomes, n = 42 NonEV proteome, independent plasma samples), with boxplot in lower panel representing protein abundance distribution. Boxplots in **A-B** show the median (centre line), 25th, 75th percentiles (box), minima and maxima within 1.5× interquartile range (whiskers), and outliers beyond. **C.** Abundance distribution of cytokines/growth factors and CD proteins quantified in pEV proteome. **D.** Heatmap of cytokines and CD proteins quantified in pEV (n = 38) and NonEV (n = 42) proteomes (independent plasma samples). Grey boxes in the heatmap represent non-quantification.





Extended Data Fig. 5 | Mapping the core proteome of pEVs and NonEVs in human. A. Heatmap of selected pEV protein features (38 individual plasma samples/ proteomes). **B.** Occurrence analysis of proteins in 38 pEV proteomes where Category 1 proteins are ubiquitously quantified (inset). **C.** Heatmap of conserved protein features in NonEVs.

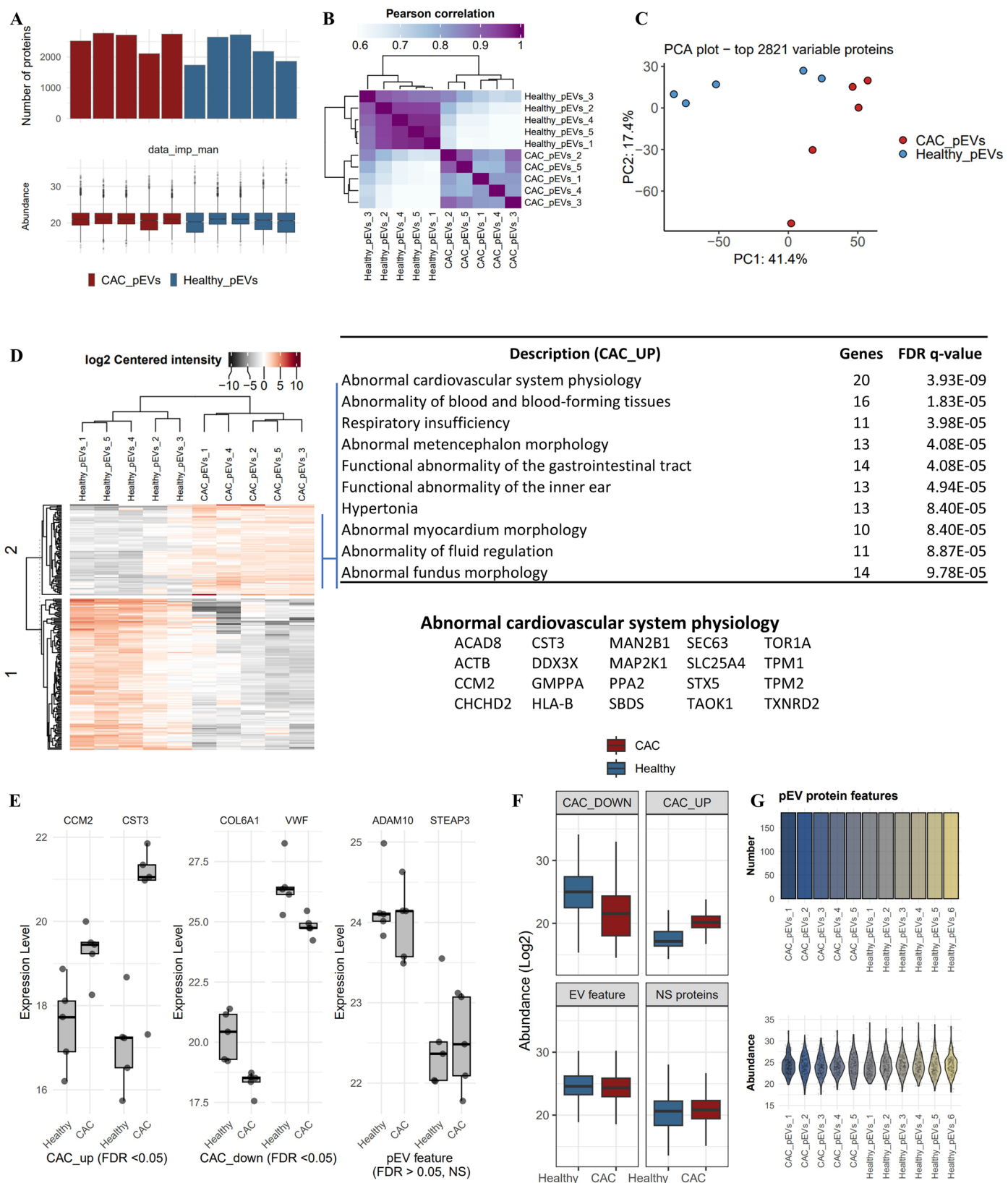


Extended Data Fig. 6 | See next page for caption.

Extended Data Fig. 6 | Coordinated molecular patterns across EV proteomes.

A. Protein–protein interaction networks of selected EV protein features (quantified in <30% of NonEV datasets) analyzed using STRING-DB and Cytoscape; each node represents a protein. Functional enrichment (GO cellular component) was performed using Cytoscape. Nodes with red border are enriched for “Extracellular exosome” term. **B.** Number of proteins belonging to coordinated molecular patterns (in Panel **A**) quantified in in vitro EVs ($n = 3$ per cell line) or EV subtypes (CD81 + , CD63 + , and CD9+ EVs) prevalent in the circulatory system⁷⁰. Quantification in MS data of individual biological replicates are shown. Lower panel shows distribution of protein abundance of these molecular features against all other proteins in their respective proteome.

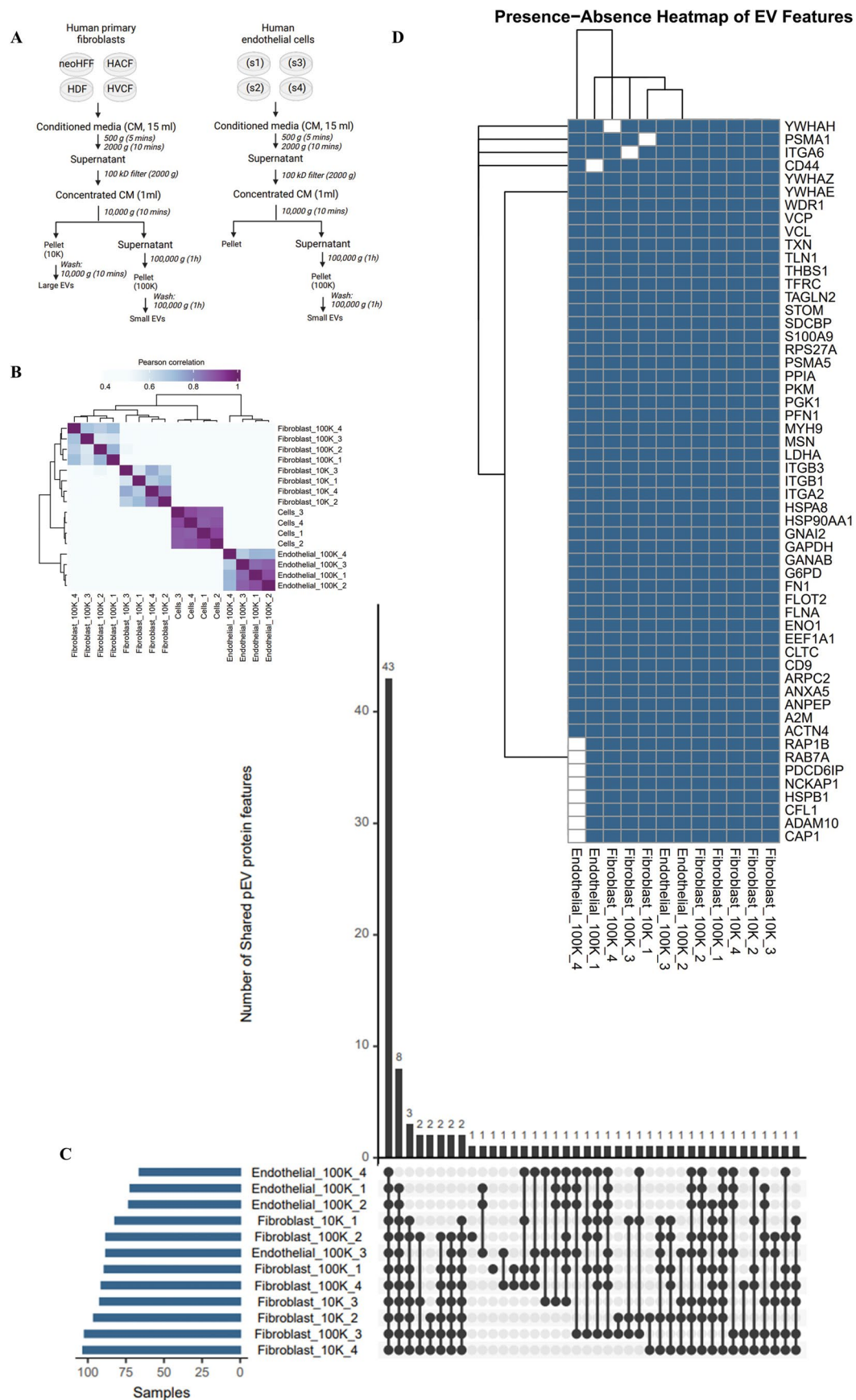
C. Number of proteins belonging to coordinated molecular patterns (in Panel **A**) quantified in small EVs (100,000 g ultracentrifuged EVs 100 K) or large EVs (10,000 g ultracentrifuged EVs 10 K) from non-transformed cells (fibroblasts). Lower panel shows distribution of protein abundance of these molecular features against all other proteins in their respective proteome. **D.** Number of proteins belonging to coordinated molecular patterns (in Panel **A**) quantified in small EVs from 14 cell lines as reported³⁰. Lower panel shows relative abundance of these molecular features in EVs versus their parental cell proteomes. Boxplot show the median (centre line), 25th-75th percentiles (box), minima and maxima within 1.5× interquartile range (whiskers), and outliers beyond.



Extended Data Fig. 7 | Proteome analysis of pEVs from individuals with either positive CAC score (CAC group) or zero CAC score (Healthy group).

A. Proteins quantified in CAC_pEVs or Healthy_pEVs (n = 5 independent plasma samples in each group). Lower panel indicates normalized proteins abundance (vsn-normalized). Boxplots show the median (centre line), 25th-75th percentiles (box), minima and maxima within 1.5× interquartile range (whiskers), and outliers beyond. **B.** Pearson correlation of quantified proteins. **C.** Principal component analysis of quantified proteins. **D.** Heatmap depicting K-means clustering of differentially abundant proteins (FDR < 0.05) in CAC_pEVs versus Healthy_pEVs: 76 upregulated and 127 downregulated proteins (FDR < 0.05), with GO pathways enriched in upregulated proteins. Proteins of the GO pathway 'Abnormal cardiovascular system physiology' are shown. **E.** Boxplot showing vsn-

normalized abundance (log2) of indicated proteins in CAC_pEVs and Healthy_pEVs proteomes (n = 5 independent plasma samples in each group). **F.** Boxplot showing distribution of either significantly upregulated (CAC_UP) or downregulated (CAC_DOWN) proteins, or non-significantly dysregulated proteins (NS proteins), and EV proteins features (EV feature) in CAC_pEVs and Healthy_pEVs proteomes (n = 5 independent plasma samples in each group). Boxplots in **E-F** show the median (centre line), 25th-75th percentiles (box), minima and maxima within 1.5× interquartile range (whiskers), and outliers beyond. **G.** pEV protein features quantified in individual CAC_pEVs versus Healthy_pEVs proteomes (n = 5 independent plasma samples in each group). Lower panel shows distribution of pEV protein features in individual proteomes. Violin plot show the distribution of vsn-normalized protein abundance (individual points are overlaid).



Extended Data Fig. 8 | Conservation of pEV protein features in EVs from non-transformed cells. A. Workflow for obtaining small EVs (100 K) or large EVs (10 K) from conditioned media of either human primary fibroblasts or human primary endothelial cells. **B.** Pearson correlation of quantified proteins in indicated proteomes using mass spectrometry. Fibroblasts (whole cell lysates) were used

as reference proteome for cells. **C.** pEV protein features quantified in small EVs (100 K) or large EVs (10 K) released by fibroblasts or endothelial cells. **D.** Heatmap indicates detection of pEV protein features in small EVs (100 K) or large EVs (10 K) released by fibroblasts or endothelial cells.





Extended Data Fig. 10 | Conservation of pEV lipid features in EVs from AusDiab validation set and in non-transformed cells. A. Principal component analysis of quantified lipids in non-transformed EVs (in vitro Small EVs or in vitro Large EVs) or pEVs, NonEVs or neat plasma from AusDiab validation set. **B.** Heatmap depicts distribution of pEV and NonEV lipid features quantified in AusDiab validation set (pEVs, NonEVs or neat plasma) and in non-transformed cell-derived EVs (in vitro Small EVs or in vitro Large EVs). **C.** Relative abundance of pEV lipid features PS(36:1) and CE(18:0) in pEVs lipidome datasets. Lipid features in

AusDiab validation set (pEVs, NonEVs or neat plasma) and in non-transformed cell-derived EVs (in vitro Small EVs or in vitro Large EVs) (n represents number of independent plasma samples/ biological replicates in each group). Bars show the group mean vsn-normalized abundance; error bars denote the standard error of the mean. Points are individual samples. One-way ANOVA was performed across groups on normalized values, followed by Tukey's multiple comparisons test (two-sided) to correct for multiple hypothesis testing. Adjusted P values (q values) are reported. Significance thresholds were set at $FDR < 0.05$.

Reporting Summary

Nature Portfolio wishes to improve the reproducibility of the work that we publish. This form provides structure for consistency and transparency in reporting. For further information on Nature Portfolio policies, see our [Editorial Policies](#) and the [Editorial Policy Checklist](#).

Statistics

For all statistical analyses, confirm that the following items are present in the figure legend, table legend, main text, or Methods section.

n/a	Confirmed
<input type="checkbox"/>	<input checked="" type="checkbox"/> The exact sample size (n) for each experimental group/condition, given as a discrete number and unit of measurement
<input type="checkbox"/>	<input checked="" type="checkbox"/> A statement on whether measurements were taken from distinct samples or whether the same sample was measured repeatedly
<input type="checkbox"/>	<input checked="" type="checkbox"/> The statistical test(s) used AND whether they are one- or two-sided <i>Only common tests should be described solely by name; describe more complex techniques in the Methods section.</i>
<input checked="" type="checkbox"/>	<input type="checkbox"/> A description of all covariates tested
<input type="checkbox"/>	<input checked="" type="checkbox"/> A description of any assumptions or corrections, such as tests of normality and adjustment for multiple comparisons
<input type="checkbox"/>	<input checked="" type="checkbox"/> A full description of the statistical parameters including central tendency (e.g. means) or other basic estimates (e.g. regression coefficient) AND variation (e.g. standard deviation) or associated estimates of uncertainty (e.g. confidence intervals)
<input checked="" type="checkbox"/>	<input type="checkbox"/> For null hypothesis testing, the test statistic (e.g. F, t, r) with confidence intervals, effect sizes, degrees of freedom and P value noted <i>Give P values as exact values whenever suitable.</i>
<input checked="" type="checkbox"/>	<input type="checkbox"/> For Bayesian analysis, information on the choice of priors and Markov chain Monte Carlo settings
<input type="checkbox"/>	<input checked="" type="checkbox"/> For hierarchical and complex designs, identification of the appropriate level for tests and full reporting of outcomes
<input type="checkbox"/>	<input checked="" type="checkbox"/> Estimates of effect sizes (e.g. Cohen's d, Pearson's r), indicating how they were calculated

Our web collection on [statistics for biologists](#) contains articles on many of the points above.

Software and code

Policy information about [availability of computer code](#)

Data collection	No software other than custom software or code was used for data collection. Software for data collection included Xcalibur software v4.0, MassHunter Acquisition v10, ZetaView (version 8.06.01 SP1), Cytek Aurora SpectroFlo (vS3.3.0)
Data analysis	No software other than custom software or code used for data collection. Software for data analysis included, GraphPad Prism software v.8.1.2/9.3.0, Image J (NIH Image Software), DIA-NN (v1.8). MaxQuant (v1.6.6.0-v1.6.14), MassHunter Quantitative Analysis 9.0, Cytek Aurora SpectroFlo (vS3.3.0), Microsoft Excel 2019 (Office365).

For manuscripts utilizing custom algorithms or software that are central to the research but not yet described in published literature, software must be made available to editors and reviewers. We strongly encourage code deposition in a community repository (e.g. GitHub). See the Nature Portfolio [guidelines for submitting code & software](#) for further information.

Data

Policy information about [availability of data](#)

All manuscripts must include a [data availability statement](#). This statement should provide the following information, where applicable:

- Accession codes, unique identifiers, or web links for publicly available datasets
- A description of any restrictions on data availability
- For clinical datasets or third party data, please ensure that the statement adheres to our [policy](#)

Data generated or analyzed during this study are included in this published article (and its supplementary information files), source data or available from Data Repositories. Lipidomics data are available from the NIH Common Fund's National Metabolomics Data Repository (NMDR) website (in addition to quantitative details in Supplementary Tables 31,40). Proteomics data are available from the ProteomeXchange Consortium. All MS-based proteomics data (including sample/label annotation) is deposited to the ProteomeXchange Consortium via the MASSive partner repository and available via MASSive with identifier (MSV000094307).

Hierarchical clustering was performed in Perseus using Euclidian distance and average linkage clustering, with missing values imputed at z-score 0. Proteome and lipidome data sets were analyzed using R package Differential Enrichment analysis of Proteomics data (DEP). Using DEP, the data was background corrected and normalized by variance stabilizing transformation (vsr, which also log2-transforms the data), followed by imputation of missing values, whereby missing at random data were 'knn' imputed and missing not at random data were 'MinProb' imputed. Protein-wise linear models combined with empirical Bayes statistics were used for the differential enrichment analysis, whereby the raw p-values were adjusted to correct for multiple testing using Benjamini-Hochberg method. Differentially abundant proteins or lipids were clustered by k-means clustering using DEP package. The PCA plot, Pearson Correlation matrix, volcano plots, log2 centred bar plots and overlap bar plots were also generated using DEP. Heatmaps were generated using ComplexHeatmap package (<https://bioconductor.org/packages/release/bioc/html/ComplexHeatmap.html>). Box plots and scatter plots were generated using RStudio package ggplot2 (https://r-squared.onlinelibrary.wiley.com/doi/abs/10.1111/j.1467-985X.2010.00676_9.x). Cytoscape was used to generate Ontology map (plugin v3.7.1). Bioconductor package clusterProfiler 4.0.23 was used to perform Ontology or KEGG pathway enrichment analysis, or gene set enrichment (KEGG) analysis, with default parameters used to identify significantly enriched gene sets. The pathway-based data integration and visualization was constructed using R package pathview. For identification of lipid-associated terms enriched in lipidomes, LION web-based ontology enrichment tool was used (www.lipidontology.com). For annotating surface proteins into different categories, SURFY-based categorical annotation of cell surface proteins were employed (<https://wlab.ethz.ch/surfaceome/>). We employed caretEnsemble R package to assess the ability of protein features (pEV protein features and NonEV protein features, using Naïve Bayes algorithm), surface protein features or lipid features, using Neural Network algorithm ('nnet')) to distinguish between pEV and NonEV particles. The Shiny web application (<https://evmap.shinyapps.io/evmap/>) powered by R and hosted on shinyapps.io, was created using the R packages shiny, gplots, and ComplexHeatmap, and offers feature selections and visualizations for EV protein and lipid feature conservations in circulating EVs.

Field-specific reporting

Please select the one below that is the best fit for your research. If you are not sure, read the appropriate sections before making your selection.

☒ Life sciences ☐ Behavioural & social sciences ☐ Ecological, evolutionary & environmental sciences

For a reference copy of the document with all sections, see nature.com/documents/nr-reporting-summary-flat.pdf

Life sciences study design

All studies must disclose on these points even when the disclosure is negative.

Sample size	Proteomic experiment/file annotation is provided in ProteomeXchange Consortium via the MASSive partner repository and available via MASSive with identifier (MSV000094307) which details the number of biological replicates for each experimental condition (at least n=3). We have further included sample annotation for all proteomic and lipidomic data acquisition in this study in Source Data 3.
Data exclusions	All data exclusions are outlined in the methods, legends and/or Source Data/Supplementary information.
Replication	For all studies, groups and analyses contained at least three independent biological samples.
Randomization	For proteomic and lipidomic sample preparations, samples were blinded and later re annotated for data analysis.
Blinding	N/A

Reporting for specific materials, systems and methods

We require information from authors about some types of materials, experimental systems and methods used in many studies. Here, indicate whether each material, system or method listed is relevant to your study. If you are not sure if a list item applies to your research, read the appropriate section before selecting a response.

Materials & experimental systems

n/a	Involved in the study
<input type="checkbox"/>	<input checked="" type="checkbox"/> Antibodies
<input type="checkbox"/>	<input checked="" type="checkbox"/> Eukaryotic cell lines
<input checked="" type="checkbox"/>	<input type="checkbox"/> Palaeontology and archaeology
<input checked="" type="checkbox"/>	<input type="checkbox"/> Animals and other organisms
<input type="checkbox"/>	<input checked="" type="checkbox"/> Human research participants
<input checked="" type="checkbox"/>	<input type="checkbox"/> Clinical data
<input checked="" type="checkbox"/>	<input type="checkbox"/> Dual use research of concern

Methods

n/a	Involved in the study
<input checked="" type="checkbox"/>	<input type="checkbox"/> ChIP-seq
<input type="checkbox"/>	<input checked="" type="checkbox"/> Flow cytometry
<input checked="" type="checkbox"/>	<input type="checkbox"/> MRI-based neuroimaging

Antibodies

Antibodies used	Details of all antibodies are provided within the data supplement. Albumin (ab207327, Abcam), AGO2 (ab186733, Abcam) were used. Mouse antibodies CD63 (556019, BD Pharmingen), CD81 (555675, BD Pharmingen), APOB100 (3715-3-250, Mabtech), APOA1 (3710-3-1000, Mabtech) were used (1:1000). For flow, Anti-ADAM 10 Antibody (Sigma-Aldrich, AB19026; 2 µg in 100 µl vol), Rabbit IgG Isotype Control (Invitrogen, 10500C) were used. Secondary antibodies used were IRDye 800 goat anti-mouse IgG or IRDye 700 goat anti-rabbit IgG (1:15000, LI-COR Biosciences). For flow, Goat Anti-Rabbit Alexa Fluor 568 Dye secondary antibody (A-11011,
-----------------	---

Validation	<p>Thermo Fisher Scientific)</p> <p>All antibodies used in this study have been validated by the manufacturer; Albumin (ab207327, Abcam) https://www.abcam.com/en-au/products/primary-antibodies/albumin-antibody-epr20195-ab207327</p> <p>AGO2 (ab186733, Abcam) https://www.abcam.com/en-au/products/primary-antibodies/argonaute-2-antibody-epr10411-ab186733</p> <p>CD63 (556019, BD Pharmingen) https://www.bdbiosciences.com/en-au/products/reagents/flow-cytometry-reagents/research-reagents/single-color-antibodies-ruo/purified-mouse-anti-human-cd63.556019</p> <p>CD81 (555675, BD Pharmingen) https://www.bdbiosciences.com/en-au/products/reagents/flow-cytometry-reagents/research-reagents/single-color-antibodies-ruo/purified-mouse-anti-human-cd81.555675</p> <p>APOB100 (3715-3-250, Mabtech) https://stella.mabtech.com/sites/default/files/product_datasheets/3715-3-250.pdf</p> <p>APOA1 (3710-3-1000, Mabtech) https://www.mabtech.com/api/files/product_datasheets/3710-3-1000.pdf</p> <p>ADAM 10 (Sigma-Aldrich, AB19026) https://www.sigmaaldrich.com/AU/en/product/mm/ab19026</p> <p>Rabbit IgG Isotype (Invitrogen, 10500C) https://www.thermofisher.com/antibody/product/Rabbit-IgG-Isotype-Control/10500C</p>
------------	---

Eukaryotic cell lines

Policy information about [cell lines](#)

Cell line source(s)	SW480 (CCL-288, ATCC), MDA MB 231 (HTB-26, ATCC), SW620 (CCL-227, ATCC) were from American Type Culture Collection (ATCC, VA, USA), and LIM1863 cells from Ludwig Institute for Cancer Research, Melbourne. Primary human cell source include human neonatal foreskin fibroblast cell line (neoHFF) [sourced as gift from P Kaur, Monash University, Australia], human dermal fibroblasts (hDF), adult (Gibco/Thermo Fisher Sci. #C0135C), human atrial cardiac fibroblasts (haCF) (Lonza, #CC-2903) and human ventricular cardiac fibroblasts (Lonza, #CC-2904), human umbilical vein endothelial cells (HUVEC, Lonza, #CC-2519; HUVEC sourced as gift [K Peter, BMDI, Australia], HUVEC-RFP, Angio-Proteomie #cAP-0001)
Authentication	Cells were grown in specified media and supplements as per detailed in methods (generation of cell conditioned media) and published protocols, and cells authenticated in our previous publications (PMID: 30582284, PMID: 23585443, PMID: 23230278, PMID: 38938901). Commercially purchased HUVEC, hDF, haCF and MDA MB 231 cells were not authenticated.
Mycoplasma contamination	Cells were routinely tested for mycoplasma (neg) contamination by PCR assay annually.
Commonly misidentified lines (See ICLAC register)	This cell line is not registered on the list of misidentified cell lines.

Human research participants

Policy information about [studies involving human research participants](#)

Population characteristics	There was no population characteristics for Red Cross plasma samples, EDCAD cohort, or AusDiab cohort (other than donation age 18 years+).
Recruitment	Red Cross plasma samples were obtained blinded as pooled plasma samples, and plasma samples from individual donors already collected in the EDCAD cohort and AusDiab cohort study used in this study. There was no criteria for participant recruitment. Clinical parameters for EDCAD plasma samples are provided in Supplementary Table 41.
Ethics oversight	Human blood plasma samples were obtained from Australian Red Cross Lifeblood or EDCAD study. For Red Cross samples, ethical permits were obtained from the ethical committee of the Australian Red Cross Blood Service Human Research Ethics Committee, and La Trobe University Human Ethics Committee (HEC19485). For EDCAD samples, ethics permit was approved through Human Research Ethics Committee (HREC) at Baker Heart and Diabetes Institute and by the Alfred Hospital Ethics Committee (EDCAD-PMS, #492/20). For AusDiab trial, ethics permit was approved through HREC at Baker Heart and Diabetes Institute and by the Alfred Hospital Ethics Committee (#39/11).

Note that full information on the approval of the study protocol must also be provided in the manuscript.

Flow Cytometry

Plots

Confirm that:

- ☒ The axis labels state the marker and fluorochrome used (e.g. CD4-FITC).
- ☒ The axis scales are clearly visible. Include numbers along axes only for bottom left plot of group (a 'group' is an analysis of identical markers).
- ☒ All plots are contour plots with outliers or pseudocolor plots.
- ☒ A numerical value for number of cells or percentage (with statistics) is provided.

Methodology

Sample preparation

Plasma EVs (~5 µg) were subjected to fixation and permeabilization using eBioscience™ Foxp3 / Transcription Factor Staining Buffer Set (Invitrogen™, 00-5523-00). Briefly, pEVs (in 50 µl PBS) was incubated with 500 µl fixation and permeabilization buffer on ice for 30 mins. Samples were ultracentrifugation at 100,000 g (1 h at 4 °C) and pellets resuspended in 100 µl wash buffer. Samples were stained with 5 µl APC Annexin V reagent (BioLegend) and either 2 µg of Anti-ADAM 10 Antibody (Sigma-Aldrich, AB19026) or Rabbit IgG Isotype Control (Invitrogen, 10500C). Samples were incubated at room temperature (gentle end-over mixing) for 1h. Samples were topped with 900 µl wash buffer and washed twice (ultracentrifuged at 100,000 g (1 h at 4 °C)) to remove any remaining antibodies and potential antibody aggregates. The pellets resuspended in 100 µl wash buffer containing 0.5 µl of Goat Anti-Rabbit Alexa Fluor 568 Dye secondary antibody (ThermoFisher Scientific) incubated for 30 mins at room temperature (gentle end-over mixing) in dark. Samples were topped with 900 µl wash buffer and washed twice (ultracentrifuged at 100,000 g (1 h at 4 °C)). Pellets resuspended in 100 µl of PBS (0.5% bovine serum albumin) filtered using 0.22 µm filter

Instrument

Cytek Aurora flow cytometer

Software

SpectroFlo (vS3.3.0)

Cell population abundance

N/A

Gating strategy

Instrument gating calibration was performed using 90 nm (#64009-15) 125 nm (#64011-15), 150 nm (#64012-15), 200 nm (#64013-15) and equal mix (90-200 nm) beads (Nanobead NIST Traceable Particle Size Standards). The threshold for side scatter was set to 430, and the gain of side scatter (SSC) were set to 10. YG3-A channel used for detecting Alex Flour 568 signal, R1-A channel used for detecting APC signal and 10 000 events were recorded for all samples with the slowest flow rate to minimize the swarming effect.

- ☒ Tick this box to confirm that a figure exemplifying the gating strategy is provided in the Supplementary Information.

Terms and Conditions

Springer Nature journal content, brought to you courtesy of Springer Nature Customer Service Center GmbH (“Springer Nature”).

Springer Nature supports a reasonable amount of sharing of research papers by authors, subscribers and authorised users (“Users”), for small-scale personal, non-commercial use provided that all copyright, trade and service marks and other proprietary notices are maintained. By accessing, sharing, receiving or otherwise using the Springer Nature journal content you agree to these terms of use (“Terms”). For these purposes, Springer Nature considers academic use (by researchers and students) to be non-commercial.

These Terms are supplementary and will apply in addition to any applicable website terms and conditions, a relevant site licence or a personal subscription. These Terms will prevail over any conflict or ambiguity with regards to the relevant terms, a site licence or a personal subscription (to the extent of the conflict or ambiguity only). For Creative Commons-licensed articles, the terms of the Creative Commons license used will apply.

We collect and use personal data to provide access to the Springer Nature journal content. We may also use these personal data internally within ResearchGate and Springer Nature and as agreed share it, in an anonymised way, for purposes of tracking, analysis and reporting. We will not otherwise disclose your personal data outside the ResearchGate or the Springer Nature group of companies unless we have your permission as detailed in the Privacy Policy.

While Users may use the Springer Nature journal content for small scale, personal non-commercial use, it is important to note that Users may not:

1. use such content for the purpose of providing other users with access on a regular or large scale basis or as a means to circumvent access control;
2. use such content where to do so would be considered a criminal or statutory offence in any jurisdiction, or gives rise to civil liability, or is otherwise unlawful;
3. falsely or misleadingly imply or suggest endorsement, approval, sponsorship, or association unless explicitly agreed to by Springer Nature in writing;
4. use bots or other automated methods to access the content or redirect messages
5. override any security feature or exclusionary protocol; or
6. share the content in order to create substitute for Springer Nature products or services or a systematic database of Springer Nature journal content.

In line with the restriction against commercial use, Springer Nature does not permit the creation of a product or service that creates revenue, royalties, rent or income from our content or its inclusion as part of a paid for service or for other commercial gain. Springer Nature journal content cannot be used for inter-library loans and librarians may not upload Springer Nature journal content on a large scale into their, or any other, institutional repository.

These terms of use are reviewed regularly and may be amended at any time. Springer Nature is not obligated to publish any information or content on this website and may remove it or features or functionality at our sole discretion, at any time with or without notice. Springer Nature may revoke this licence to you at any time and remove access to any copies of the Springer Nature journal content which have been saved.

To the fullest extent permitted by law, Springer Nature makes no warranties, representations or guarantees to Users, either express or implied with respect to the Springer nature journal content and all parties disclaim and waive any implied warranties or warranties imposed by law, including merchantability or fitness for any particular purpose.

Please note that these rights do not automatically extend to content, data or other material published by Springer Nature that may be licensed from third parties.

If you would like to use or distribute our Springer Nature journal content to a wider audience or on a regular basis or in any other manner not expressly permitted by these Terms, please contact Springer Nature at

onlineservice@springernature.com